Chemical Science

ROYAL SOCIETY OF CHEMISTRY

REVIEW

View Article Online
View Journal

Cite this: DOI: 10.1039/d5sc10189a

Challenges and advances of sulfide solid electrolytes for high-energy-density sodium metal batteries

Kaizhi Chen,†[a] Haohua Jiang,†[a] Hongyu Li,[a] Xiang-Long Huang,[a] Kunjie Zhu,[a] Long Yao,[a] Weihong Lai[b] and Yun-Xiao Wang *[a]

With high ionic conductivity and excellent mechanical properties, sulfide solid electrolytes (SSEs) represent a leading candidate electrolyte system for sodium metal batteries (SMBs), offering enhanced energy density and improved safety. However, the development and practical deployment of SSEs are hindered by intrinsic air instability, poor interfacial compatibility with electrodes, and demanding synthesis conditions. This review provides a comprehensive summary aimed at accelerating the adoption of SSEs in high-energy-density sodium metal batteries. We systematically examine the crystal structures and properties of sulfide sodium-ion conductors, followed by critical challenges related to air stability, electrode–electrolyte interfaces, and synthesis techniques. Subsequently, effective strategies for realizing high ionic conductivity, improved chemical/electrochemical stability, and enhanced interfacial compatibility have been thoroughly summarized and discussed. When coupled with different cathodes, the interfacial challenges and long-term cycling stability of SSE-based sodium metal batteries (SSE-SMBs) were further discussed. Besides, the advantages and challenges of different cathodes at high energy densities are also mentioned. Finally, taking the cathode, SSEs, and anode into account, we identify the challenges of these electrode materials and the areas for improvement to achieve high energy densities.

Received 30th December 2025
Accepted 9th March 2026

DOI: 10.1039/d5sc10189a

rsc.li/chemical-science

1 Introduction

As a promising supplement to lithium-ion batteries (LIBs), sodium-ion batteries (SIBs) have attracted considerable research interest owing to their lower cost.[1–6] Despite their relatively low energy density, SIBs are regarded as an ideal candidate for large-scale electrochemical energy storage. Meanwhile, sodium metal batteries (SMBs) have emerged as an even more attractive system by replacing conventional intercalation-type anodes with a sodium metal anode. Boasting an ultrahigh theoretical specific capacity of 1165 mAh g^{-1},[7–11] SMBs can achieve an energy density more than 50% higher than that of SIBs.

However, the development of high-energy-density SMBs faces fundamental challenges in long-term safety, primarily due to the use of liquid organic electrolytes and the nature of sodium metal itself. Liquid organic electrolytes generally suffer from a narrow electrochemical stability window and high flammability.[12–15] Issues such as self-discharge, leakage, and corrosion further raise concerns over battery lifespan and serious safety hazards in case of short circuits. Moreover, the high reactivity of sodium metal, its unlimited volume change during stripping/plating, and the severe growth of sodium dendrites in organic electrolytes pose additional critical obstacles. Fortunately, replacing liquid electrolytes with solid-state electrolytes has revived the prospect of developing safe and high-energy-density SMBs.[16–19]

The commercial development of solid electrolytes (SEs) requires a balanced optimization of ionic conductivity, manufacturing cost, interfacial compatibility, and chemical/electrochemical stability.[20–23] Currently, the SEs mainly include oxides, sulfides and halides, and these various electrolytes have their own merits and challenges. Among these, oxide-based solid electrolytes are particularly notable for their excellent air stability and can be prepared without the protection of an inert atmosphere. However, their ionic conductivity is relatively low. For example, $Na_3Zr_2Si_2PO_{12}$, a representative NASICON-type oxide, has become a research focus due to its moderate ionic conductivity (10^{-3} S cm^{-1}), high mechanical strength, and exceptional environmental stability. When used in SMBs, its high mechanical strength can effectively serve as a shield to restrain dendrite growth. However, the high-valent cations in $Na_3Zr_2Si_2PO_{12}$ are thermodynamically unstable upon contact with highly reductive metallic sodium, leading to the spontaneous formation of an interfacial decomposition

[a]Institute of Energy Materials Science (IEMS), University of Shanghai for Science and Technology, Shanghai 200093, China. E-mail: yunxiaowang@usst.edu.cn
[b]Laboratory of Advanced Materials, Shanghai Key Laboratory of Molecular Catalysis and Innovative Materials, School of Chemistry and Materials, Fudan University, Shanghai 200433, China
† These authors contributed equally to this work.

layer. This layer mainly consists of Na_2O, ZrO_2, and amorphous silicon- and phosphorus-rich compounds, which significantly increase the interfacial impedance and impede Na^+ ion transport across the electrode–electrolyte interface.[24–26] The synthesis of $Na_3Zr_2Si_2PO_{12}$ requires the use of costly precursors, high heating temperatures, and long heating times, which result in a substantial increase in manufacturing costs. Halide-based electrolytes exhibit superior ionic conductivity and are compatible with high-voltage cathodes, showing potential for high-energy-density SMBs, but the insulating NaCl generated from the direct contact between sodium and halide electrolytes is detrimental to sodium ion diffusion. The continuous accumulation of NaCl affects the diffusion path, causing uneven sodium deposition and uncontrollable dendrite expansion, and ultimately worsening the durability of all solid-state sodium metal batteries (ASSMBs).[27–29] Furthermore, several promising halide systems, such as Na_3YCl_6 (10^{-4} S cm^{-1}) and Na_3TaCl_6 (10^{-3} S cm^{-1}), rely on rare and expensive elements such as yttrium and scandium, raising concerns about long-term scalability and cost-effectiveness for large scale battery production.[30–32] Sulfide solid electrolytes (SSEs) stand out as the optimal choice for commercial solid-state electrolytes because of their high ionic conductivity (which can even reach 10^{-2} S cm^{-1}) and reasonable manufacturing costs. When exposed to air, SSEs rapidly react with moisture in the air to produce toxic H_2S gas, which causes the decomposition of the electrolyte's structure and a reduction in ionic conductivity. Moreover, the reduction reaction between SSEs and metallic sodium leads to the formation of a high impedance interfacial layer, which is detrimental to ion diffusion. The poor air stability and interface compatibility of SSEs hindered their commercial production.[33–35] Strategies such as element doping or replacement, composite design, and interfacial modification can improve air stability while retaining the inherent advantage of outstanding ionic conductivity. Additionally, the constituent elements (S, P, Sb, and Sn) used for synthesizing sulfide electrolytes are abundant, which favors cost control for electrolyte production. Considering all these factors, the adoption of SSEs can meet both the requirements of economic benefits and performance, and they are regarded as potential candidates for ASSMBs. Numerous reviews have been reported previously, but they predominantly focus on material preparation and structural configuration while often overlooking progress toward high specific energy in full-cell applications. By focusing on the critical interplay between material design and full-cell performance, a review with this unique perspective is urgently required to provide more practical guidance for the development of SSE-SMBs.

In this review, we systematically outline the classification, transport mechanisms and critical challenges of SSEs, followed by a discussion of optimization strategies developed for cathode, anode and electrolyte materials to improve air stability, ionic conductivity and interfacial compatibility. We also summarize practical application protocols and battery performance of various SSE-SMBs, and mainly focus on the electrochemical performance when paired with different cathode materials. This review clarifies the key parameters, challenges and optimization pathways of SSEs, providing useful references and research insights to facilitate the commercialization of high-energy-density SSE-SMBs.

2 General structures and properties of sulfide sodium-ion conductors

2.1 Crystal structure and composition

Based on the structural formula, SSEs can be classified into two types: Na_xMS_y ($x = 3, 4, 5$; $y = 3$, 4/M = P, Sb, *etc.*) and $Na_zM_2PS_{12}$ (z = 11 or 12/M = Si, Ge, Sn, *etc.*). Obviously, the difference between the two configurations of SSEs mainly lies in the content of Na and S. The details will be mentioned as follow:

2.1.1 Na_xMS_y (x = 3,4,5; y = 3,4/M = P, Sb, *etc.*). Based on the Na_xMS_y configuration, a series of SSEs can be designed. For example, Na_3SbS_4 (NSS), a classical Na_xMS_y-type SSE, exhibits a crystal structure characterized by body-centered SbS_4^{3-} tetrahedra connected by sodium ions (Fig. 1a).[36] The diffusion channels of sodium in the [010] plane are displayed on the right side. Sodium ions can diffuse along multiple dimensions, which manifests as the high ionic conductivity of NSS. Then, novel electrolyte configurations are derived through variations in sodium content, encompassing both increased and decreased sodium concentrations. As displayed in Table 1, Na_4SiS_4, Na_5AlS_4 and Na_4SnS_4 electrolytes can be obtained through the regulation of sodium content. Furthermore, element doping has a positive impact on ionic conductivity of SSEs. Whether this change is beneficial or detrimental mainly depends on the type and content of the doping and replacing elements.

2.1.2 $Na_zM_2PS_{12}$ (z = 11 or 12/M = Si, Ge, Sn, *etc.*). Evolving from $Li_{10}GeP_2S_{12}$, the $Na_zM_2PS_{12}$-type SSEs also possess excellent ionic conductivity, but there are differences in the crystal structures. Distinct with LGPS, the sodium ions that located in the NGPS lattice only occupy octahedral vacancies, which can account for the large lattice volume (almost four times that of LGPS).[37] Within the crystal structure of $Na_{11}Sn_2PS_{12}$, displayed in Fig. 1b, Na ions can undergo rapid diffusion along a three dimensional (3D) ion diffusion channel network, which manifests as the high ionic conductivity and low activation energy of $Na_{11}Sn_2PS_{12}$. Sodium ions undergo migration *via* a portion of the sodium vacancies. Moreover, $Na_{10}SiP_2S_{12}$, $Na_{10}GeP_2S_{12}$, and $Na_{10}SnP_2S_{12}$, have also been designed, which share the same crystal structure. It is noteworthy that the progression from Si and Ge to Sn brings about a marginal augmentation in activation energy. This phenomenon can be observed in both sodium-

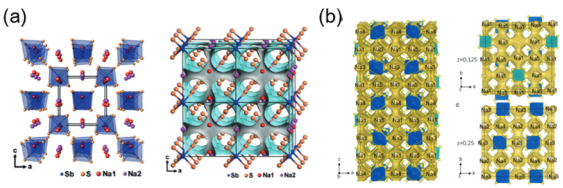

Fig. 1 (a) The crystal structure and 3D bond valence map of Na_3SbS_4.[36] Copyright 2016, John Wiley and Sons Ltd. (b) The crystal structure of $Na_{10}SnP_2S_{12}$.[37] Copyright 2018, RSC.

Table 1 Electrochemical properties of Na_xMS_y type electrolytes

Electrolytes	Ionic conductivity (mS cm^{-1})	Activation energy (kJ mol^{-1})	Ref.
Na_3PS_4	0.20	27.89	38
Na_3SbS_4	0.44	25.77	39
Na_3AsS_4	0.03	32.91	38
Na_3BS_3	0.011	39	40
Na_4SiS_4	0.02	36.67	41
Na_5AlS_4	0.00032	33.77	41
Na_3InS_3	0.0068	42.46	42
Na_4SnS_4	0.000014	52.19	43
Na_4SnSe_4	0.000022	20.27	43
Na_3PSe_4	1.16	20.27	44
$Na_3P_{0.62}As_{0.38}S_4$	1.46	24.70	38
$Na_{2.85}P_{0.85}W_{0.15}S_4$	8.8	27.41	45
$Na_{2.8}PS_{3.8}Cl_{0.2}$	0.09	22.2	46
$Na_{2.8}SbS_{3.8}Cl_{0.2}$	2.17	23.35	39
$Na_{2.85}SbS_{3.85}Br_{0.15}$	2.87	18.82	39
$Na_{2.85}SbS_{3.85}I_{0.15}$	1.22	22.97	39
$Na_{3.06}Sb_{0.94}Si_{0.06}S_4$	0.68	26	47
$Na_{3.06}Sb_{0.94}Ge_{0.06}S_4$	0.01	32	47
$Na_{3.06}Sb_{0.94}Sn_{0.06}S_4$	0.02	35	47
$Na_{3.06}Sb_{0.88}Mo_{0.12}S_4$	3.9	21	47
$Na_{3.06}Sb_{0.88}W_{0.12}S_4$	32	17.08	48
$Na_{2.88}Sb_{0.88}W_{0.12}S_{3.8}O_{0.2}$	3.6	23.16	49
$Na_3SbP_{0.16}S_{3.6}O_{0.4}$	3.82	95.63	50
$Na_4Sn_{0.67}Si_{0.33}S_4$	0.01	54.04	51
$Na_{3.1}Ge_{0.1}Sb_{0.9}S_4$	5.1	15.05	52
$Na_3PS_{3.85}O_{0.15}$	0.27	41.69	53
$Na_{3.5}SnS_{3.5}Br_{0.5}$	0.02	39.57	54
$Na_{3.6}Sn_{0.8}P_{0.2}S_{3.8}Cl_{0.2}$	0.22	31.85	54
$Na_{3.8}Sn_{0.9}P_{0.1}S_{3.9}Br_{0.1}$	0.51	28.95	54
$Na_{3.7}Sn_{0.9}Sb_{0.2}S_{3.9}Br_{0.1}$	0.42	26.06	54
$Na_{3.7}Sn_{0.9}Sb_{0.2}S_{3.9}Cl_{0.1}$	0.64	25.09	54
$Na_{3.7}SnS_{3.7}Cl_{0.3}$	0.00036	47.29	54
$Na_{2.8}Zn_{0.8}Ga_{1.2}S_4$	0.08	30.88	55

based and lithium-based materials, and the ionic conductivity of SSEs synthesized based on Si and Ge is higher than that based on Sn.[56] Moreover, other $Na_zM_2PS_{12}$-type and derived SSEs are listed in Table 2.

2.2 Ion-transport mechanism

The operation of SSE-SMBs relies on the directional migration of ions through SEs, and the diffusion rate can be reflected by ionic conductivity, while high ionic conductivity corresponds to rapid ion transport in SEs. When it comes to the diffusion of single atoms, the interstitial and vacancy theories can provide explanations. As displayed in Fig. 2a, the interstitial mechanism refers to lattice ions that are originally located at interstitial sites jumping between adjacent interstitial positions to realize long-range migration by active or passive approaches. The active approach illustrates ions spontaneously jumping to adjacent interstitial sites. Then, the passive approach occurs when the ion transportation requires the assistance of other ions and simultaneously induces the transportation of the next ion. The vacancy mechanism can be expressed as one ion jumping to the adjacent vacancy and creating a new vacancy at the original position. It is noteworthy that the vacancy diffusion requires two conditions: sufficient vacancy concentration and adequate activation energy for the ion to overcome the migration barrier. Actual diffusion processes should not be confined to single ion migration, because the practical ion diffusion predominantly occurs through multiple atom diffusion, indicating that the diffusion mechanisms of ions are typically more complex.

Table 2 Electrochemical properties of $Na_zM_2PS_{12}$-type electrolytes

Electrolytes	Ionic conductivity (mS cm^{-1})	Activation energy (kJ mol^{-1})	Ref.
$Na_{10}SiP_2S_{12}$	10.28	22	57
$Na_{10}GeP_2S_{12}$	3.5	26.05	57
$Na_{10}SnP_2S_{12}$	0.4	34.35	57
$Na_{10.8}Sn_{1.9}PS_{11.8}$	0.67	29.91	58
$Na_{11}Sn_2PS_{12}$	1.4	24.12	59
$Na_{10}SnSb_2S_{12}$	0.52	22.19	60
$Na_{11}Sn_2AsS_{12}$	0.11	39.56	61
$Na_{11}Sn_2SbS_{12}$	0.56	32.8	62
$Na_{11}Sn_2SbS_{11}Se$	0.34	35.7	62
$Na_{11}Sn_2SbSe_{12}$	0.15	37.63	62
$Na_{11}Sn_2Sb_{0.5}Ti_{0.5}S_{12}$	1.01	26.05	63

From Fig. 2b, the improvement of ion diffusion can be achieved within the help of vacancy creation, concerted migration, lattice polarizability, anion disorder, and lattice expansion. The fluctuation of lattice volume was mainly attributed to the size of the doped atom. For example, replacing P^{5+} with Sb^{5+} in Na_3PS_4 (NPS) will expand the lattice volume, which can be attributed to the higher radius of Sb^{5+}.[64] Notably, the ionic conductivity and air stability of NSS both witnessed a significant enhancement when compared with NPS. The substitution of Sb^{5+} with W^{6+} will bring about abundant Na vacancies and boost the transformation of the crystal structure; thus, ionic conductivity will be enhanced.[48,65]

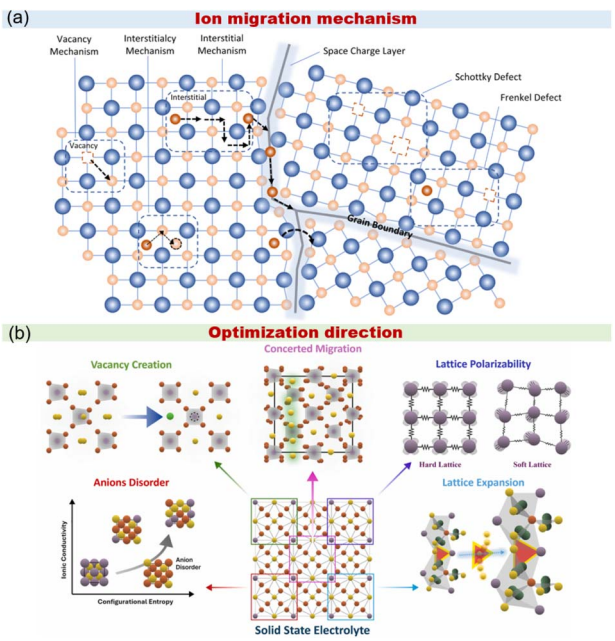

Fig. 2 (a) The diffusion of ions in solid electrolytes.[66] Copyright 2023 RSC and (b) the strategies of diffusion improvement.[67] Copyright 2025 Elsevier BV.

Anion disorder is not considered a crystal defect but rather an intrinsic material characteristic. In solid-state electrolytes, it is primarily influenced by configurational entropy and elemental doping. When employing other chalcogenide ions, such as Se^{2-} or Te^{2-}, to replace S^{2-}, lattice softening can be induced, and the migration energy can be obviously reduced.[68]

3 Critical challenges of sulfide solid electrolytes

For large-scale production, the preparation of SEs should be equipped with the characteristics of low cost and simple preparation. As discussed in current investigations, the preparation cost of SEs should not exceed \$50 per kg.[69,70] Li_2S, as a key synthetic raw material for lithium-based SSEs, has relatively high costs, which can be attributed to the influence of preparation processes, application prospects, and trade markets. When using Li_2S as the raw material to prepare SSEs, the increased manufacturing costs caused by raw materials are not suitable for large-scale production. Sodium-based SSEs fabricated with Na_2S as the starting material have garnered significant attention from researchers. This is because China is the world's largest producer of Na_2S; thus, when selecting Na_2S as the raw material to participate in the synthesis of Na-based SSEs, the preparation cost can be controlled within an acceptable range and is not sensitive to changes in the external environment. The reduction in SSE production costs is beneficial for promotion; however, several challenges still exist in the commercialization of SSE-SMBs.

3.1 Demanding preparation conditions

Currently, the preparation of SSEs requires the combination of proportioning, ball-milling and heating processes. The pre-

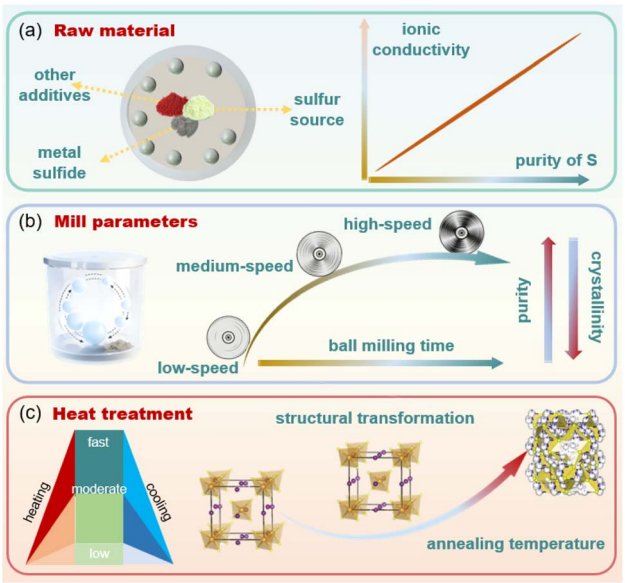

Fig. 3 The influence of the (a) raw material, (b) ball milling process and (c) heat treatment on SSEs.[74] Copyright 2016 RSC.[75] Copyright 2022 Elsevier.

design of SSE configurations can be realized by modifying the weight ratios of raw materials, that is, reducing the proportions of sulfur precursors or metal sulfides and elevating the proportions of additive phases associated with elements targeted for doping or replacing (Fig. 3a). Researchers deeply believe that ball milling and heat treatment processes are key factors affecting the performance of SSEs, but the influence of raw materials on SSEs is often overlooked. Taking NPS as an example, NPS with identical crystal phases exhibits substantial variations in ionic conductivity due to differences in preparation methods. Most studies tend to attribute these variations simply to impurities introduced during synthesis or raw material purity, without conducting in-depth investigations into the underlying mechanisms. The influence of Na_2S purity on the ionic conductivity of SSEs has been explored by Janek *et al.*[71] For convenient identification, the following designations were assigned: Na_2S-d for industrially dried Na_2S, Na_2S-p for additionally purified Na_2S, and Na_2S-c for commercially available anhydrous Na_2S. XRD results reveal that an obvious distinction between Na_2S-d, Na_2S-p and Na_2S-c lies in the unique Na_2SO_x peak that exists in Na_2S-c. When Na_2S-c was used for NPS preparation, the product after ball milling was displayed in an amorphous type and required subsequent heat treatment to obtain the tetragonal NPS. In contrast, the tetragonal phase NPS can be obtained by the adoption of Na_2S-p or Na_2S-d through a simple ball milling method. Further analysis revealed that during the synthesis process, oxygen from Na_2SO_x impurities tends to combine with P to form P–O bonds, which are harmful to the crystallization of NPS. Notably, the ionic conductivity of NPS that selects Na_2S-c as the raw material cannot compete with that of NPS prepared using other raw materials. The ionic conductivity of NPS exhibits an upward trend with the elevation of the heat treatment temperature, but is still less than 0.04 mS cm^{-1}.

Zeier *et al.* further investigated the effects of the milling process on the structure and electrochemical performance after SSE preparation.[72] With a long ball milling time, SSE powders with fine particles and high purity can be obtained, but the extension of milling time inevitably reduces the crystallinity of SSEs and makes the crystal structure disordered (Fig. 3b). Moreover, a long-term ball milling time will increase the consumption of electrical energy and production costs. Therefore, it is necessary to find a moderate ball milling time to maximize cost savings while ensuring high purity. The introduction of disordered structures can both meet the need for providing low-energy diffusion pathways, reducing the energy barrier for ion diffusion, and boosting the ion migration through a synergistic effect, which is beneficial for achieving efficient ion transformation. However, excessive disorder can disrupt the connectivity of the ion transport network, leading to a decrease in conductivity.[73] The purity of SSEs was related to the milling time, and the crystal structure of SSEs is mainly affected by the annealing temperature.

Within an annealing temperature of 250 °C, the ionic conductivity and activation energy are only 0.77 mS cm^{-1} 0.42 eV. When the annealing temperature has not exceeded 300 °C, the crystal structure of NPS was presented in the cubic

phase, and the increase in annealing temperature will promote the transformation of the crystal structure. 300 °C can serve as the phase inversion temperature from the cubic phase to the tetragonal phase. Then, the peak intensity of tetragonal NPS becomes more obvious when the temperature keeps increasing and eventually becomes stable at 450 °C. The ionic conductivity and activation energy can reach 15.5 mS cm^{-1} and 0.40 eV, respectively.[74] Researchers generally believe that there are only two configurations of NPS (tetragonal and cubic). However, Christian's team revealed that there also exists an orthorhombic structure of NPS (γ-Na_3PS_4) when the temperature reaches 510 °C.[76] The optimal ionic conductivity (400 mS cm^{-1}) and activation energy (0.11 eV) can be obtained. The mainstream research mostly focuses on exploring the effects of milling speed and heating temperature on SSEs, while the influence of cooling rate is rarely mentioned. As reported by Strauss *et al.*,[77] the cooling rate can directly affect the microstructure of SSEs after the annealing process. Faster cooling rates may lead to the formation of non-equilibrium phases or metastable phases in SSEs, whereas slower cooling rates allow more atoms to rearrange, forming an ordered and higher crystallinity microstructure. The addition of microstructures may lead to an increase or decrease in ionic conductivity, which mainly relies on the physical or chemical properties of the microstructure. Concludingly, the structural transformation of NPS is not an abrupt change, but a gradual process that is strongly associated with the ball milling and heat treatment processes, and this crystal change can be well exhibited in Fig. 3c. Hence, the significance of processing temperature cannot be ignored.

3.2 Intrinsic material instability

As discussed in hard and soft acid–base (HSAB) theory, the ratio difference between charge density and particle radius is usable for classifying acids and bases. According to this principle, acids with a low ratio of charge density to atomic radius are defined as soft acids. Soft acids preferentially bind to soft bases (which share the same characteristic) *via* covalent bonding, while the interaction between hard acids and hard bases is dominated by ionic bonding or electrostatic interactions.[78] In phosphorus-containing SSEs, S^{2-} contained in the PS_4^{3-} unit is oxidized to a higher valence state and eventually forms $P_2S_7^{4-}$ or $P_2S_6^{2-}$. These species can react with hard Lewis acids (H^+) to generate toxic H_2S gas (Fig. 4a), and the volume of H_2S evolved is directly proportional to the humidity of the ambient air. Additionally, the crystal structure of SSEs witnessed a significant change, from PS_4^{3-} to $PS_{4-x}O_x^{3-}$, which is accompanied by an increase in diffusion resistance and a decrease in ionic conductivity.[79–81] The HSAB theory offers an intuitive understanding of the high sensitivity of SSEs in air, particularly in moisture environments.

3.3 Unstable and incompatible interfaces

Thanks to the remarkable plasticity of SSEs, a compact interfacial contact can be obtained, which is beneficial to reduce interfacial impedance and boost the diffusion of Na ions. However, the narrow electrochemical window of SSEs imposes

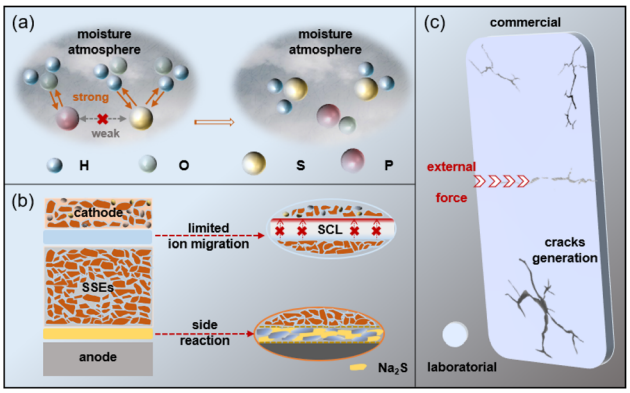

Fig. 4 (a) The mechanism of H_2S generation in phosphorus-containing SSEs; (b) schematic illustration of critical interfacial issues between sulfide electrolytes and both cathode and anode electrodes; (c) key translational challenges in scaling sulfide solid electrolytes from laboratory research to industrial production.

restriction on cathode selection. When the operating voltage is greater than 2.5 V, nonconductive phases, such as S, PS_x, P_2S_5, S–O and P–O bonds, will be generated along with the decomposition of NPS.[82,83] Moreover, the adoption of high voltage cathodes presents a high electrochemical potential; thus, alkali metal ions spontaneously migrate from low electrochemical potential to high electrochemical potential, specifically diffusing from SSEs to the cathode. When ion diffusion reaches a threshold, a space charge layer (SCL) is generated at the interface between the cathode and SSEs, which multiples the interfacial resistance.[84–86] For example, the undesirable outcomes (Na_3PO_4, $NaCrS_2$, and the intermediate phase Na_3PSO_3) generated from the contact between NPS and the $NaCrO_2$ cathode results in a limited capacity (60 mAh g^{-1}).[87] In addition, the preparation of the cathode employed in SSE-SMBs mainly relies on mechanical mixing active materials with SSEs and conductive carbon. This simple mixing method cannot eliminate the interfacial difference and eventually causes a decline in battery capacity.[88–90]

Notably, the interfacial issues are not only present on the cathode side; the adoption of metallic sodium on the anode side makes interface issues more prominent. Owing to the large ionic radius of Na, the inferior binding energy cannot restrain the external electron, thereby imparting high chemical activity to Na. Thus, the undesirable side reactions that occur with the contact of Na and SSEs worsen the durability of SSE-SMBs. For example, the interface between NPS and metallic Na cannot remain stable after the direct contact of the electrode, and the reaction formula can be described as follows:

$$8Na + Na_3PS_4 \rightarrow 4Na_2S + Na_3P$$

Continual reaction increases the amount of insulated Na_2S, and the accumulation of Na_2S multiples the diffusion resistance of Na^+, resulting in a high overpotential. Moreover, the continual reaction between SSEs and metallic sodium will intensify the consumption of sodium sources. Then, the volume

variation that caused by the formation of side-reaction products damages the integrity of the contact interface, deteriorates the interfacial contact and worsens the durability of SSE-SMBs. The interfacial issues between SSEs and the cathode/anode illustrated in the above paragraphs can be well exhibited in Fig. 4b.

3.4 Scalable challenges

During large-scale production, the dosage of raw materials is far more than in laboratory production, which raises the difficulty to ensure the purity of SSEs during the preparation. Otherwise, the assembly of SSE-SMBs requires external pressure to achieve interfacial contact among various materials. However, the tablets pressed in the laboratory remain small in size, which cannot meet the demand of commercial production. Hence, scalable powder compaction technology should be developed, which is crucial for the efficiency and integrity of SEs (Fig. 4c). The minor defects that exist in laboratory-assembled SSEs will reduce the durability of SSE-SMBs. Furthermore, the challenges posed by internal defects in the electrolyte become more severe when the area of SEs has increased by several times. Furthermore, the brittleness of SSEs increases with the size, which means that SEs can only withstand limited external impact forces. Once the external impact force becomes excessive, SEs will break. Therefore, the large-scale production of SSEs requires corresponding large-area pressure application devices.

4 Strategies for electrolyte design and interfacial engineering

To advance the commercialization of SSEs, researchers have adopted various optimization strategies, which can be broadly categorized into two mainstream approaches: modification of SSEs themselves and changes in their external environment. Herein, we will elaborate on this in detail below:

4.1 Bulk modification

Inspired by the HSAB theory, the optimization of SSE air stability can be realized by introducing "hard" components to protect or replace "soft" sulfur to reduce the preferential binding between S^{2-} and H^+, thereby inhibiting the generation of H_2S.

4.1.1 Elemental doping or replacing. The choice of highly acid cations (Ca^{2+}, Mn^{2+}, Sn^{2+}, Zn^{2+}, Ga^{3+}, *etc.*) can better reduce the reaction tendency between S^{2-} and H^+ dissociated from the water molecules in an air atmosphere. This is because the binding force on S^{2-} is greater than the inductive force of H^+, which manifests as an improvement in air stability. For example, Adams's team employed Ge^{4+}, Ti^{4+}, and Sn^{4+} to partially replace P in Na_3PS_4.[91] Ulteriorly, metal cations with higher acidity can further replace P for dual doping. Compared with Na_3PS_4, completely replacing P with Sb in NSS can enhance both ionic conductivity and air stability. Dai *et al.* doped germanium on the basis of NSS.[52] It is noteworthy that substituting Sb^{5+} with lower-valent Ge^{4+} creates sodium interstitial defects in the crystal lattice. Within the introduction of interstitial defects, the ionic conductivity of $Na_{3.1}Ge_{0.1}Sb_{0.9}S_4$ was higher than that of undoped NSS. When exposed to a humid environment, the H_2S extraction of germanium-doped $Na_{3.1}Ge_{0.1}Sb_{0.9}S_4$ was lower than NSS (almost 54.5%). Moreover, XPS analysis indicated that the signal change of $[SbS_4]$ in $Na_{3.1}Ge_{0.1}Sb_{0.9}S_4$ is difficult to observed, which indicated that germanium doping helps to enhance the air stability of NSS without sacrificing ionic conductivity. In the design of doping hard acids on the cation side, especially in multi-ion composite doping, which elements should be selected as the dominant elements? Does it follow any design principles? These questions are worthy of further exploration.

The method of ionic doping in SSEs should not be limited to the cation side; replacing weakly basic S^{2-} with hard base anions is also an effective approach to improve air stability. According to the HSAB theory, the optimal combination should be hard acid–hard base or soft acid–soft base. When hard bases (O^{2-}, Cl^-, Br^-, *etc.*) are added to SSEs, H^+ tends to combine with the hard bases, thereby protecting S^{2-} sufficiently. Consequently, the air stability of SSEs can be improved. Guided by the above principle, Yao *et al.* replaced S with a small amount O (<0.6).[53] With the addition of oxygen, the formed P–O chemical bonding was stronger than P–S; the stronger bonding significantly enhanced the mechanical strength of $Na_3PS_{4-x}O_x$. Then, sintering the $Na_3PS_{4-x}O_x$ SSEs at room temperature caused the transformation into a fully homogeneous glass structure and possessed robust mechanical properties. Additionally, the air stability and interfacial compatibility can be enhanced by the addition of O elements. Distinct with the modified SSEs, the direct contact of Na and NPS leads to the generation of insulated Na_3P and Na_2S_x,[92] which appear at the interface in the form of a black phase. The reduction of the black phase can be viewed in the NPS sample with 0.25% O (NPSO25) pieces. Furthermore, no obvious black phase can be observed in the NPS sample with 1% O (NPSO1) pieces, even under prolonged surface contact time.

4.1.2 Composite electrolyte engineering. Combining mechanical and chemical stability into SSEs, Yao's team employed a composite design to prepare "sandwich-typed" SSEs.[53] The inner $Na_3PS_{3.85}O_{0.15}$ layer has an advantage in ionic conduction, and the outer $Na_3PS_{3.4}O_{0.6}$ layer displays remarkable mechanical and chemical stability to meet the need for alleviating parasitic reactions and limiting dendrites. Similarly, Janek *et al.* employed $Na_{3.4}Zr_2Si_{2.4}P_{0.6}O_{12}$ (NZSPO) as a buffer layer to avoid the detrimental reaction between NSS and Na (Fig. 5a).[93] The NZSPO can also couple with $Na_{2.9}Sb_{0.9}W_{0.1}S_4$ prepared by W addition and Na to improve the interfacial stability. It is well known that the ionic conductivity of oxide SEs was insufficient; thus, the composite electrolyte fabricated by the lamination method induces an increase in interfacial impedance when an oxide layer is added to the interface. Based on the same combination of SEs, Tatsumisago *et al.* took NZSPO as the dominant material and NPS as additives to fabricate composite electrolytes.[94] The mixing of SSE particles with different ionic conductivities does not cause the deterioration of overall ionic conductivity but enhances the stability efficiently. The ionic conductivity of composite electrolytes can be further improved by replacing NSS with NPS (Fig. 5b),[95] which

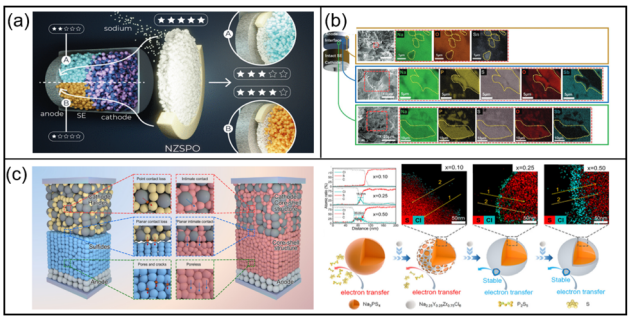

Fig. 5 (a) The schematic illustration of composite electrolyte design by constructing oxide electrolyte interface layers to ease side reactions between sulfides and anodes.[93] Copyright 2023 American Chemical Society. (b) Composite sulfide electrolytes with other sulfide electrolytes.[95] Copyright 2022 Wiley VCH. (c) Mixing halide electrolytes and sulfide electrolytes to form a halide coating layer on the surface of sulfide electrolytes.[100] Copyright 2025 John Wiley and Sons Ltd.

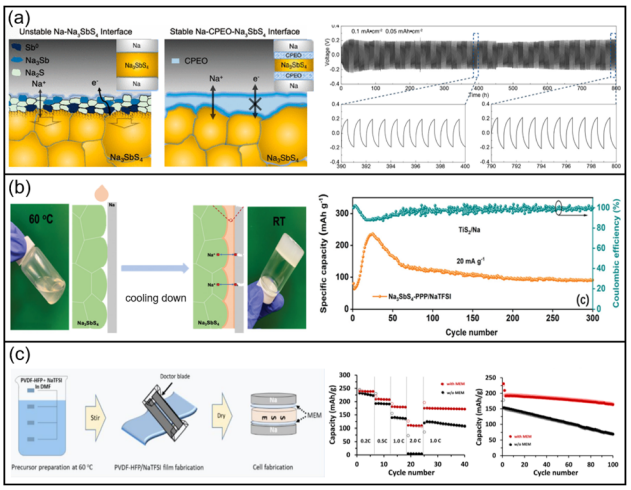

Fig. 6 (a) Schematic diagram of the CPEO-passivated anode interface (left) and the corresponding performance of the symmetric cell (right).[101] Copyright 2019 American Chemical Society. (b) Temperature-regulated modification of the anode–electrolyte interface by a PPP passivation layer (left) and the corresponding full cell performance (right).[102] Copyright 2021 Wiley VCH Verlag. (c) Schematic of the MEM layer protecting the anode–cathode interface and the corresponding rate and cycling stability of the full cell.[103] Copyright 2024 Elsevier Ltd.

may be explained by the space charge effect. Notably, the ionic conductivity changes with the ratio of NSS and NZSPO. The composite electrolytes that combined different SSEs, such as NPS–Na_4SiS_4,[96] NPS–NSS,[36] NPS–$Na_{10.8}Sn_{1.9}PS_{11.8}$,[97] NPS–$Na_{11}Sn_2SbS_{11.5}Se_{0.5}$,[98] NPS–$Na_{12}Sn_2PSe_{12}$,[99] 2NSbS–$Na_2WS_4$ and 2NSS–Na_4XS_4 (X = Si, Ge, Sn)[90] have also been reported in existing research.

In particular, the combination of sulfides and halides has been successfully designed by the milling method. After ball milling, the $Na_{2.25}Y_{0.25}Zr_{0.75}Cl_6$ halides can serve as a coating layer for NPS (Fig. 5c),[100] which can bring about an increase in oxidative stability, ionic conductivity and Young's modulus. Beneficial to the special design of the core–shell structure, the conduction of Na^+ can be achieved on multiple scales. When coupled with a $NaNi_{0.33}Fe_{0.33}Mn_{0.33}O_2$ cathode, the capacity of SSE-SMBs can remain 76.4 mAh g^{-1} at 2C.

4.2 Surface passivation/coating interface

Obviously, the adoption of metallic sodium can increase battery capacity, but the inherent high chemical reactivity inevitably triggers side reactions with the electrolyte and boosts the formation of a passivation layer. The introduction of the passivation layer makes ion diffusion more difficult. When sodium metal anodes are applied in batteries, surface modification is often required to ensure stable operation. From Fig. 6a, Yao's team designed a cellulose–poly ethylene oxide (CPEO) interlayer to stabilize the interface between NSS and Na.[101] The CPEO layer can both meet the dual purpose of conducting ions and blocking electrons. When testing the symmetrical batteries at 0.1 mA cm^{-2}/0.05 mAh cm^{-2}, the lifespan can be extended to 800 h without a significant change in overpotential. Wang *et al.* combined poly ethylene glycol, poly propylene glycol and poly ethylene glycol (PEG–PPG–PEG) with sodium salt (NaTFSI) to prepare an amphiphilic triblock copolymer (Fig. 6b), which can self-assemble into micelles to optimize the interface.[102] When heated to 60 °C, PPP is displayed in a liquid state; the fluid state allows it to closely link the electrode and electrolyte interface. The design of the PEG–PPG–PEG (PPP) copolymer can increase the toughness and viscosity of the polymer. The ASSSBs that consist of Na, TiS_2 and PPP electrolytes remain at 100 mAh g^{-1} specific capacity after 300 cycles.

As displayed in Fig. 6c, a 4 μm-thick NaTFSI/PVDF-HFP membrane (MEM) has been successfully fabricated as an interface layer to prevent the undesirable decomposition between Na and SSEs.[103] The addition of sodium salts can enhance ionic conductivity but cannot compete with LEs. To reduce the interfacial contact resistance, batteries using polymer coatings need to operate at a high temperature (60 °C) to promote the transition of the polymer from the solid phase to the liquid phase. However, the flowing polymer causes uneven distribution of components and different ion diffusion rates at various directions, ultimately cause uneven deposition and dendrite growth. Notably, the deficiency of mechanical strength makes the polymer unstable to restrain dendrite development efficiently; thus, the operation of polymer coatings was inapplicable to high stripping/plating systems. Beneficial to the protection of the MEM film, the full cell exhibited remarkable rate performance and a small capacity decline. Even after 100 cycles at 1C, the cell within the protection of MEM film still remains at 167 mAh g^{-1}, with a capacity retention rate of nearly 86%, which is higher than that of the cell without MEM protection (less than 50%).

Element doping involves the introduction of cations or anions into the lattice of SSEs, which can expand the channels for ion migration and increase the carrier concentration, thereby enhancing the ionic conductivity and stability. The process is relatively simple and can be completed in a single step during the material synthesis stage. However, it is crucial to ensure a moderate doping concentration. That is because a low amount of

dopant elements fails to yield any improvement, and an excessive doping amount may lead to incomplete reactions and the formation of impurity phases. Interfacial engineering involves introducing an artificial protective layer at the interface. This layer can prevent harmful side reactions and provide a stable interface for ion transport; thus, the interface compatibility and cycling stability can be improved. However, the presence of the coating layer may introduce additional impedance, and the uniformity cannot be guaranteed, especially under large-scale production. The design of composite electrolytes can be realized by physically mixing or stacking two or more electrolyte materials. It is worth noting that the simple mixture of electrolytes does not mean that their respective advantages will be superimposed; the distribution and orientation of the mixed phases severely affect its performance. Taking above strategies into comparison, element doping is mainly used to improve ionic conductivity. However, in large-scale synthesis, the uniformity of element doping is difficult to precisely control, leading to large variations between different batches. Moreover, certain doping elements (such as Ge and Se) can significantly increase production costs, which does not meet the requirements for commercialization. Composite electrolytes serve as the optimal carrier for engineering implementation, but it is necessary to select appropriate components for compounding to mitigate the negative impact of non-conductive or low-conductive components on the ionic conductivity of the electrolyte. Coating a passivation layer on the surface of sulfide electrolytes can effectively improve air stability and interfacial compatibility and exerts little influence on the existing production system; thus, it is regarded as a key technology for the transition from laboratory research to mass production. However, the coating process needs further optimization to improve coating uniformity and prevent excessive local impedance from impairing ionic transport. The large-scale preparation of SSEs does not rely on a single approach; instead, multiple strategies are implemented in parallel. Specifically, elemental doping is first used to optimize the base material, followed by surface passivation to improve air stability and suppress interfacial side reactions. Finally, scalable production is realized through compounding sulfide with other types of electrolytes.

4.3 Anode interface optimization

Aiming to reduce the reactivity of metallic Na, the design of an artificial SEI (ASEI) is regarded as a valid strategy to alleviate the interfacial side reaction.[104–106] At present, the ASEI can be prepared using a pre-treated Na anode or generated *in situ* interface *via* the spontaneous reaction between Na and SSEs, which helps reduce side reactions and enhance cycling stability. Otherwise, the design of alloy anode had been employed to optimize the interface between anode and electrolytes. As follows, we will demonstrate the details of various reaction-stabilized interfaces.

4.3.1 Pre-treated Na anode. Sebastian used Na-β″-Al_2O_3 as a buffer layer between Na and Na_3PS_4.[107] The Na-β″-Al_2O_3 was insensitive to both Na and Na_3PS_4; thus, the addition of the Na-β″-Al_2O_3 buffer layer can restrain the decomposition efficiently. Similarly, Sun's team prepared an alucone film by the molecular layer deposition technique, which is beneficial to maintain the stability of interface (Fig. 7a).[108] When operating in a long-term, the surface coated with the alucone film remains flatter without significant colour changes, which can be attributed to the positive effect of the alucone film in ion diffusion and dendrite limitation. As exhibited in Fig. 7b, Tu *et al.* successfully established a NaF-rich ASEI on the Na surface by the dripping method.[109] The addition of NaF prevents the direct contact between SSEs and Na metal, thereby reducing the incidence of undesirable reactions. Moreover, the NaF component enhances the interfacial strength and positively suppresses the expansion of dendrites. Thus, the lifespan of symmetric cell can be extended to 800 h with the assistance of NaF at 0.1 mA cm^{-2}/0.1 mAh cm^{-2}.

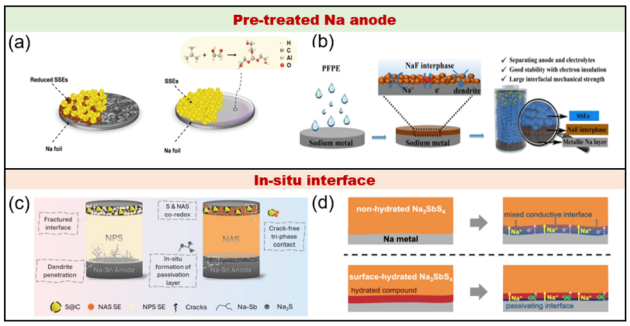

Fig. 7 The pre-treated Na anode by reacting Na metal with (a) alucone.[108] Copyright 2020 Wiley VCH Verlag, and (b) perfluoropolyether (PFPE).[109] Copyright 2024 Elsevier. The *in situ* interface formation at anode/solid electrolyte contacts for (c) NSS.[110] Copyright 2025 RSC, and (d) NSS·$8H_2O$.[111] Copyright 2019 Elsevier.

4.3.2 *In situ* interface. It is widely accepted that the parasitic reactions that occur with the direct contact of Na and SSEs severely affect the cycle performance of SSE-SMBs. Skilfully, Zhao *et al.* modified the interface within an *in situ* reaction between the Na–Sn alloy and NSS (Fig. 7c).[110] Compared with the interface in NPS, the Na_3Sb alloy-containing interface demonstrates superior performance in dendrite inhibition and interface integrity. Thus, the overpotential of NSS was smaller than NPS, which further indicated that the alloy component can further decrease the diffusion resistance. In addition, the inherent high mechanical strength of NSS plays an active role in dendrite propagation. Thus, SSE-SMBs equipped with NSS can operate at a high current density (0.5 mA cm^{-2}). Maintaining consistency with NSS, Ceder's team further regulated the electrode–electrolyte interface through the adoption of surface-hydrated NSS (Fig. 7d).[111] The reaction equations between NSS and its aqua compound are compared as follows:

$$8Na + Na_3SbS_4 \rightarrow 4Na_2S + Na_3Sb$$

$$44Na + Na_3SbS_4 \cdot 8H_2O \rightarrow 4Na_2S + Na_3Sb + 16NaH + 8Na_2O$$

$$44Na + Na_3SbS_4 \cdot 8H_2O \rightarrow 4Na_2S + Na_3Sb + 18NaH + 9Na_2O$$

It is not difficult to find that the interfacial reactions involving hydrate species contribute to compositional

diversification. From a thermodynamic perspective, NaH and Na_2O are insensitive to metallic Na. The introduction of NaH and Na_2O can passivate the interface because of their high ionic conductivity and electronic resistivity. Increasing the degree of hydration elevates the concentrations of NaH and Na_2O but causes a decline in ionic conductivity. Concludingly, moderate concentrations of NaH and Na_2O provide beneficial contributions, while excessive amounts negatively impact ionic diffusion. Innovatively, the interfacial reaction can be beneficial when strategically employing electrolyte and anode self-sacrificial mechanisms, offering performance enhancement rather than deterioration, thereby providing pioneering guidance for future investigations. In addition, the above research studies make us realize that the interfacial stability should not be regarded as the only criterion for evaluating the electrochemical performance of SSE-SMBs.

4.3.3 Alloy anodes. Anode materials targeting high-energy-density applications should demonstrate both accelerated charge/discharge rates and reliable durability. However, the large ionic radius of Na^+ leads to a sluggish kinetics and limited ion migration efficiency.[112,113] When applied at high current densities, issues such as fragile SEI, uncontrollable Na dendrite expansion, and huge volume expansion are further exacerbated. The stable operation of SSE-SMBs requires an even distribution of Na^+ flux to reduce the tendency of uneven deposition. When Na protrusions emerge on the Na surface, Na^+ tends to accumulate around the prominent area and induce dendrite generation. The rampant expansion of Na dendrites eventually penetrates the separator and causes battery failure by linking the cathode and anode. "Sand time" represents the critical period in electrodeposition from current initiation to the complete depletion of metal ions at the cathode surface, triggering dendrite formation. Current density serves as the dominant factor, where elevated current densities can reduce sand time and exacerbate the generation of sharp dendrites. Additionally, the assembly of SSE-SMBs requires the application of external pressure. However, the soft Na may penetrate into the electrolyte under external force, which significantly increases the risk of short circuits. The alloy anode possesses higher mechanical strength when stamped into slices. The design of alloy anodes, such as Na–Sn, Na–Sb, or other alloys, is known for their high specific capacity but is limited by their volume expansion. When assembled in SSE-SMBs, the issue of volume expansion can be improved under external force. The alloy anode employed in SSE-SMBs is the Na–Sn alloy. Other alloy anode designs have rarely been reported, and the role of various alloy anodes in improving energy density of SSE-SMBs deserves further investigation and supplementation by researchers.

4.4 Cathode interface regulation

In contrast to the solid–liquid interfacial contact characteristic of liquid phase batteries, SSBs predominantly rely on solid–solid interfacial contact, which cannot meet the need for interfacial wettability. The repeated stripping/plating process can further deteriorate the loss of contact area and eventually damage battery capacity. To improve the issues that exist at the SSE–cathode interface, the following methods have been employed:

4.4.1 Cathode coating. Shaijumon *et al.* added a succinonitrile–PVDF-HFP–$NaClO_4$ (SPN) membrane as a coating layer to avoid the direct contact between SSEs and the cathode.[114] The organic layer should be coupled with a high operating temperature to ensure a compact surface. Specifically, the strategy of heating the sample to ensure compact contact both applies to SSE powders. As exhibited in Fig. 8a, a NPS coating layer was successfully formed on CMK-3.[115] The annealing process will boost the precipitation of Na_2S, which can plug the meso-channels (4 nm) in CMK-3 and further improve the tightness of the interfacial fit. When operating at 60 °C, the batteries displayed a high capacity of 810 mAh g^{-1} in the first cycle and still remained at 650 mAh g^{-1} after 50 cycles. Similarly, a NSS-coated S cathode was successfully prepared by Hayasi's team.[116] After

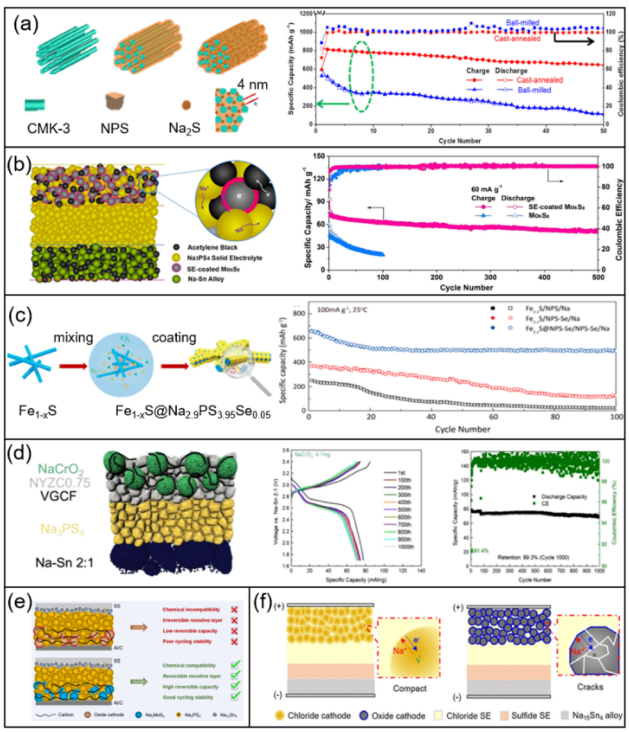

Fig. 8 (a) Schematic of NPS/Na_2S cathode coating on CMK-3 *via* thermal annealing (left) and the corresponding electrochemical performance (right) of NPS.[115] Copyright 2018 American Chemical Society. (b) The schematic diagram of a solid-electrolyte coated Mo_6S_8 cathode (left) and the related full cell performance (right).[117] Copyright 2018 American Chemical Society. (c) Schematic diagram of coating NPSSe on the surface of the $Fe_{1-x}S$ cathode (left) and the corresponding electrochemical curves of the full battery (right).[118] Copyright 2018 American Chemical Society. (d) Coating the outside of the $NaCrO_2$ cathode with halides to improve the interfacial contact with sulfide electrolyte (left) and the related electrochemical performance (right).[119] Copyright 2018 Springer Nature. (e) The schematic illustration of a cathode prepared by the mixture of C, NPS and Na_2MoS_4.[120] Copyright 2025, Wiley-Blackwell. (f) The design of an all-in-one cathode without the addition of a conductive phase and sulfide electrolytes.[121] Copyright 2025, American Chemical Society.

simple mixing and ball-milling the NSS solvents and MSP20, a NSS interface layer can be introducing into the S cathode, which is beneficial to enhance the compatibility of the cathode and NSS electrolytes. Thus, the batteries showed a high initial capacity (1560 mAh g^{-1}) and a slow capacity decline of only 5% after 50 cycles. Furthermore, Wang's team used *N*-methylformamide (NMF) to dissolve NPS particles.[117] The cathodic Mo_6S_8 was immersed in this solvent and further dried to obtain an NPS-coated cathode. Distinct from the direct contact between NPS and Mo_6S_8, the coating design prepared by liquid solvent methods can introduce an even NPS layer on the Mo_6S_8 surface (Fig. 8b) and significantly improve the interfacial contact between Mo_6S_8 and SSEs. Similarly, a $Na_{2.9}PS_{3.95}Se_{0.05}$ layer also can be generated by liquid methods, and the preparation can be viewed in Fig. 8c.[118] A cathodic $Fe_{1-x}S$ encapsulated with $Na_{2.9}PS_{3.95}Se_{0.05}$ can improve the durability of SSE-SMBs. Even after 100 cycles at high current density (100 mA g^{-1}), the capacity remains at an acceptable value (494.3 mAh g^{-1}).

4.4.2 Composite with SSEs. Due to the terrible interface stability between SSEs and cathodic powders, researchers proposed a strategy of coating the cathode with other electrolytes. Fig. 8d illustrates that the $NaCrO_2$ particles were covered by $Na_{3-x}Y_{1-x}Zr_xCl_6$ (NYZC),[119] which is insensitive to $NaCrO_2$. Even at a high heating temperature (220 °C), no new phase can be detected in the mechanical mixture of NYZC and $NaCrO_2$. Thus, the batteries can operate stably for 1000 cycles with a small capacity decline rate. Unlike liquid electrolytes that can flow and accommodate volume variations of cathodic S well, the infiltration of powered SSEs was insufficient and cannot meet the need of filling the interparticle gaps resulting from cathode expansion and contraction, which worsens the interfacial contact on the cathode side and further leads to the decline of capacity. When SSEs are mixed with the S/C composition, the substantial volume changes associated with sulfur redox processes can be alleviated, thereby supporting the long-term structural integrity of the whole structure. Tatsumisago *et al.* systematically compared the electrochemical performance of S-KB-P_2S_5 and S-KB-Na_3PS_4.[122] The results indicated that the capacity of S-KB-Na_3PS_4 is higher than that of S-KB-P_2S_5. The available mixing degree served as the key factor to explain capacity enhancement. Zhao's team mixed S/C with NPS or NSS to use as the cathode.[110] The testing results indicated that the higher capacity can be attained within the combination of S/C/NSS, NSS and $Na_{15}Sn_4$. Then, the SSE-SMB capacity that consists of S/C/NPS, NPS and $Na_{15}Sn_4$ was less than 1000 mAh g^{-1}, and along with poor cycle stability. Aiming to avoid the inferior interface compatibility between SSEs and oxide cathodes, Vlad *et al.* employed Na_2MoS_4 as the cathode to match with NPS (Fig. 8e),[120] which possesses outstanding chemical and electrochemical stability. Thus, cathodic Na_2MoS_4 can be mechanically mixed with NPS and carbon without any decomposition. Consequently, the full cell equipped with Na_2MoS_4 displayed reversible capacity(188 mAh g^{-1}) at 0.3 C and high capacity retention rate (nearly 100%) after 450 cycles. Taking the above results into consideration, we speculated that the capacity increase of SSE-SMBs is not sensitive to the mixing degree but depend on the mixed SEs. The product derived from physical mixing of cathodic S with SSEs could potentially serve as an additional capacity source within the SSE-SMBs.

4.4.3 All-in one design. Typically, a cathode mainly consists of active material, conductive additives and binder. In SSE-SMBs, a compact interface can be realized under the function of external force, which can eliminate the addition of binder. The presence of inactive constituents in SSE-SMBs limits the diffusion path and adversely affects energy density and interfacial properties. The addition of inactive SEs is essential for boosting ion transportation, but it inevitably reduces the ratio of cathode material and results in limited energy density. The discrepancies in ionic conductivity among different particles generate uneven ion migration rates, thereby multiplying the tortuosity of diffusion pathways. All-in-one cathode designs have been conceived to circumvent the challenges associated with inactive constituents. That is because the all-in-one cathode displays outstanding ionic and electronic conductivity, simultaneously. The subsequent table systematically summarizes the documented implementations of all-in-one cathodes applied in SSE-SMBs:

Hayashi's team prepared Na_3NbS_4 as a cathode to couple with the Na–Sn alloy and NPS.[123] It is noteworthy that the structure of Na_3NbS_4 was affected by milling speed and milling time. After ball milling at 510 rpm for 10 h, the resulting Na_3NbS_4 exhibits an amorphous phase. With increasing rotation speed and ball milling time, the crystal structure transforms from an amorphous phase to a metastable phase. Then, the prolonged holding process at 700 °C induces a transformation into the orthorhombic phase. When couple with the Na–Sn alloy, the highest capacity can be obtained by adopting metastable phase I in the cathode side. Similarly, the

Table 3 The application of all-in-one cathodes in SSE-SMBs

Cathode	Crystal structure	Capacity (mAh g^{-1})	Voltage range	Voltage platform	Ref.
Na_3NbS_4	Amorphous	210	0.8–3.2	1.7	126
	Metastable phase I	240	0.8–3.2	1.6	126
	Metastable phase II	180	0.8–3.2	1.6	126
	Orthorhombic	50	0.8–3.2	1.7	126
Na_2TiS_3	Amorphous	250	1.2–2.7	1.7	127
	Cubic rocksalt	270	0.8–3.2	1.7	127
Na_2FeS_2	Cubic spinel-type	320	0.7–3.2	1.8	128
$NaFeCl_4$	—	117	2.65–3.95	3.4	129

crystal structure of Na_2TiS_3 varies with different rotation speeds.[124] It is noteworthy that the crystal structure change from amorphous to cubic rocksalt not only raises the capacity but also broadens the operating window. Moreover, a cubic spinel-type Na_2FeS_2 cathode has been further proposed.[125] The addition of cathodic Na_2FeS_2 can enhance battery durability, displaying a high capacity retention rate after operating for 300 cycles at 0.255 mA cm^{-2}. Specifically, the halide can also serve as the cathode to fit with SSEs. The issues, such as crack advance and interface contact failure that accompany with the volume expansion of layered oxide cathode, can be improved by the replacement of a $NaFeCl_4$ cathode (Fig. 8f).[121] The design of $NaFeCl_4$ is equipped with the merits of high ductility and stability. Accompanied by the insertion of Na^+, $NaFeCl_4$ can change into Na_6FeCl_8 (Suzuki-type), $Na_{1.38}Fe_{1.31}Cl_4$ (orthorhombic spinel-type), and Na_2FeCl_4 (cubic spinel-type structure), and the initial structure can be returned when Na is extracted completely from the cathode, which indicates that the structure of $NaFeCl_4$ displays remarkable reversibility during the plating/stripping process. Hence, the full cell can operate stable for 500 cycles at a high rate (2C) without significant capacity decline. For easy comparison, we list the detailed parameters of the above integrated cathodes in Table 3.

5 Advancing manufacturing and scalability

Currently, Wu's group made the first report on the research regarding the gas phase synthesis of $Li_4SnS_{4.2}$.[130] It is noteworthy that the preparation can be executed in an atmospheric environment. The selection of raw materials also has the advantages of air stability and low cost. Nonetheless, CS_2 employed in gas phase synthesis has an inescapable tendency to generate toxic waste gas during the synthesis procedure, which requires the optimization of waste gas treatment devices. Furthermore, there are relatively few research reports on gas-phase synthesis of Na-typed SSEs, which can be attributed to their high reactivity, and exposure to the atmosphere inevitably results in the decomposition of Na-typed SSEs. Thus, the fabrication of SSEs mainly relies on solid or liquid-phase methods. While the solid-phase synthesis of SSEs surely boosts purity and ionic conductivity, its low efficiency can't meet mass-production needs. The liquid-phase method can serve as an effective complement in SSE synthesis, because the liquid-phase method enables the mixing of raw materials at the molecular level and offers advantages such as low reaction temperature, controllable product size and morphology, and ease of achieving continuous production. When made into a large-area film, SSEs become fragile and sensitive to external force, which cannot meet the need for scalable production. Thus, the scalable production of SSEs should be combined with PTFE to attain a pliable film. Moreover, the density can be further intensified by secondary compaction.

5.1 Solution-based processes

Using a liquid-phase approach to synthesize SSEs, the selection of liquid solvents mainly includes organic and aqueous solvents. SSEs can be obtained by the centrifugation and heat treatment of precursor solvents. The organic solvent, such as *N*-methylformamide (NMF),[131] methyl acetate (MA),[132] 1,2-dimethoxyethane (DME) and diethyl ether (DEE),[133] are also mentioned as solvents to prepare Na_3PS_4. Unlike the high melting point of NMF, the adoption of DME and DEE, which possess low melting points (<100 °C), will reduce the difficulty of subsequent residual solvent treatment. It is well known that the diameter of Na^+ was greater than Li^+, which results in the deficiency of charge density on the Na^+ surface; thus, the solvents should be equipped with a higher donor number to promote the reaction between Na_2S and P_2S_5 in organic solvents. Thus, the adoption of MA solvent can well meet the above demand because of its high donor number (16.3 kcal mol^{-1}). After dissolving and heating the solvents that include Na_2S and P_2S_5, NPS powders can be attained. Notably, the undesirable side reactions between NPS and organic solvents inevitably introduce new phases into the final products, which may cause a decline in ionic conductivity. Furthermore, the preparation of SSEs can also be realized with the help of aqueous solution. For example, NSS[134,135] and $Na_{3-x}Sb_{1-x}W_xS_4$ (ref. 136) can be obtained by adding the raw material into water and heating at a proper temperature to remove the water. With the addition of S, Na_2S and Sb_2S_3,[134] the bisulfide anions (HS^-) generated by the dissolution of Na_2S in H_2O can further react with the sulfur-rich anion (SbS_3^{3-}) in Sb_2S_3 and S to boost the generation of the fundamental framework (SbS_4^{3-}) of NSS. Although the addition of acetone was beneficial to accelerate the generation of precursor powders, the precipitation of H_2S will be aggravated. The difference between organic solvents and aqueous solvents in the synthesis of SSEs is illustrated in Fig. 9a and b, where the generation of bubbles corresponds to the release of H_2S. Aqueous solvent-based synthesis of SSEs carries the risk of material hydrolysis and is only applicable to specific SSEs. In contrast, organic solvents suffer from insufficient solubility of raw materials, and the issue of residual solvent after synthesis still remains to be resolved.

5.2 Tape-casting for thin membranes

To pursue high energy density, SSEs should tend towards thin-film fabrication. The design of SSE films can minimize the proportion of inactive materials and effectively harness the potential of high-capacity electrodes (such as manganese-based cathodes, silicon–carbon anodes and metallic anodes). The design of films holds the potential to effectively address the challenge of insufficient toughness encountered in SSEs. With

Fig. 9 Illustration of the liquid phase method for preparing SSEs with (a) organic and (b) aqueous solvents.

the tiny addition of PTFE, flexible and processable thin films can be achieved (Fig. 10a),[137] which can be attributed to the fibrous network of PTFE. Even under relatively low external stacking pressure, SSE thin films can maintain intimate contact with the electrodes. Specifically, PTFE displays inherent electrochemical inertness, which means that PTFE will not participate in battery redox processes. The porous and continuous ion-conductive network formed by PTFE helps to intensify ion transport kinetics. During the fabrication of SSE-SMBs, the interfacial contact area between the electrode and SSEs is limited to merely 5–6%, which severely hinders ion diffusion. To improve the inherent solid–solid interfacial contact issues, isostatic pressing techniques are employed, which prove beneficial for enhancing the densification and structural integrity of the contact interfaces and further increasing the ionic conductivity. Isostatic pressing represents a forming and densification technique within the help of fluid medium (liquid or gas) to apply uniform high pressure onto the material. Based on processing temperature variations, isostatic pressing can be categorized into cold isostatic pressing (room temperature), warm isostatic pressing (<250 °C), and hot isostatic pressing (>900 °C).

From Fig. 10b, the SEM image disclosed that the initial morphology of NPS and $Na_{2.5}PS_{3.5}F_{0.5}$ (NPSF) particles was irregular.[138] Under an applied pressure of 156 MPa, the interparticle voids within NPS gradually diminish, and a small number of holes can be observed when the pressure reaches 389 MPa. Obviously, the surface of NPSF remains smooth at 156 MPa, and progressive enhancement of interfacial densification can be achieved with incremental pressure application. The pressure–relative density graph well illustrated that the density increases with the external force. Moreover, the EIS outcome indicated that the diffusion resistance of NPS and NPSF both witnessed a decline along with external force, and the change in NPS was larger than that in NPSF. This can be attributed to the inherent high ductility of NPSF, which is not sensitive to the variation of applied force when the densification process reaches a critical threshold. Currently, cold isostatic pressing and warm isostatic pressing have been successfully employed in SSE preparation,[140–142] whereas hot isostatic pressing was rarely mentioned. That is because the metal–sulfur (M–S) bonds in SSEs stem from the inherent thermal lability and pronounced volatility. Thus, the undesirable thermal decomposition, volatilization phenomena, and exacerbated interfacial parasitic reactions will be deteriorated under elevated thermal conditions.[143–147] It is noteworthy that not all microstructural variations induced by densification are beneficial.[148] While reductions in pore size and crack length enhance the critical current density (CCD), increases in pore spacing and crack narrowing conversely diminish the CCD. The large-scale fabrication of sodium foil faces several critical challenges: (1) highly reactive sodium metal should be stored away from air, moisture and electrophiles; (2) weak sodium–sodium bonding forces result in tearing during deformation processes; (3) sticky metallic sodium will cause significant adhesion due to interfacial friction during the rolling process. As exhibited in Fig. 10c, pieces of meter-scale sodium metal foil with thicknesses ≤50 μm and high mechanical strength have been successfully fabricated by Wang's team,[139] which mainly relies on the introduction of polydimethylsiloxane (PDMS). The introduction of PDMS effectively mitigates interfacial friction resistance during the rolling process of sodium metal, thereby enhancing the processing performance of the anode material. Moreover, some PDMS forms covalent bonds with sodium *via* Si–O linkages, establishing a flexible-inorganic bilayer SEI. This configuration not only enhances the elastic modulus of the sodium foil but also facilitates interfacial sodium ion diffusion and promotes uniform deposition. Thus, a high energy density (180.2 Wh kg^{-1}) can be realized within the combination of sodium and diethylene glycol dibutyl ether.

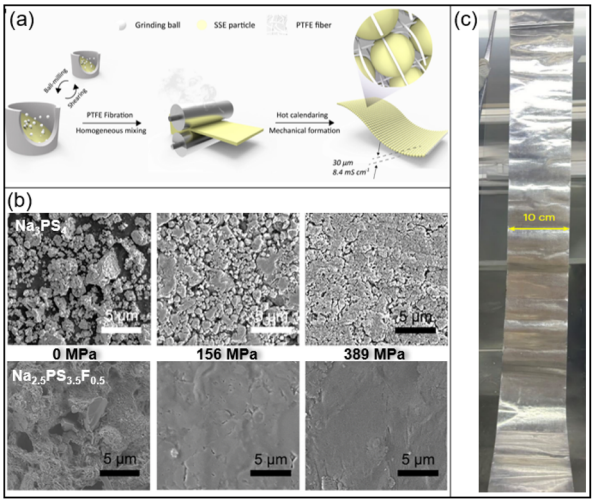

Fig. 10 (a) Preparation of the PTFE film.[137] Copyright 2021 American Chemical Society. (b) The evolution of surface morphology under external pressure.[138] Copyright 2025 RSC. (c) Optical image of the large-scale Na film.[139] Copyright 2025 Springer Nature.

6 Compatible sodium battery systems and energy density

Battery energy density is a key indicator for judging commercial battery performance, which represents the amount of energy that can be stored per unit volume or unit mass. Mass energy density refers to the amount of energy that stored per unit mass of a battery and is typically expressed in Wh kg^{-1}. The energy density can be calculated using the following equation:

$$\text{Energy density (Wh kg}^{-1}\text{)} = \text{Specific capacity (mAh g}^{-1}\text{)} \times \text{Voltage (V)}$$

The improvement of energy density can be achieved by increasing the operating voltage or capacity. The operational voltage is determined by the intrinsic properties of the material and the characteristics of the electrode interface.

Capacity enhancement can be achieved by utilizing high-capacity electrode materials (metallic anodes, silicon anodes, high-voltage layered oxides and transformative cathodes).[149] Limited by the slow reaction kinetic and volume expansion, the

inherent benefits of silicon anodes fail to be realized within sodium batteries. Given the constrained scope for advancement at the metal anode, the improvement of energy density was predominantly concentrated on the cathode side. Herein, we mainly provide a brief overview of existing solid-state sodium battery cathode systems in the following section.

6.1 High-voltage oxide cathodes

Oxide cathodes are famous for their high operating voltage, thus, the addition of adoption of oxide cathodes can raise the energy density. For example, Hayashi's team selected $NaCrO_2$ as the cathode to couple with NPS.[87] The capacity is only 60 mAh g^{-1} but with a high operating voltage (2.9 V). Replacing NPS with NSS, the initial capacity witnessed a significant increase and can reach 200 mAh g^{-1}.[150] Even after 20 cycles, the capacity retention rate remains at 85%, but the operating voltage dropped to 1.7 V. The increase in capacity may be accounted by the improvement of interfacial compatibility between the $NaCrO_2$ cathode and SSEs. However, the limited electrochemical window cannot meet the need for a high operating voltage and tends to decompose into an insulating phase. The formation of SCL, induced by the chemical potential difference between SSEs and oxide cathodes, increases the resistance to ionic migration. Accordingly, when employing oxide cathodes, a protective or passivation layer must be introduced to prevent direct contact between SSEs and oxide cathodes, which inevitably increases the total mass of the cell and reduces the gravimetric energy density of SSE-SMBs. That is to say, the presence of SCL severely hinders the practical application of oxide cathodes.

Surprisingly, Ma *et al.*[151] demonstrated that the large grain boundary resistance of $Li_{0.33}La_{0.56}TiO_3$ originates from the grain boundary core rather than the SCL. Electron microscopy observations reveal that the SCL near grain boundaries is rich in alkali metal ions and carries positive charge, while the grain boundary core is a lithium-deficient region. Furthermore, both theoretical calculations and electrochemical results confirm that the SCL does not impede ion movement but instead plays a positive role in the ion migration process. Notably, existing studies on the SCL between oxide cathodes and SSEs mainly focus on carrier concentration rather than atomic-scale structure. Thus, it remains to be further explored whether atomic-scale SCL analysis developed for other systems is applicable to SSE systems, and this research will significantly promote the application of oxide cathodes in high-energy-density SSE-SMBs.

6.2 Polyanion cathodes

Thanks to the high operating voltage plateau of $Na_3V_2(PO_4)_3$ (NVP), researchers have attempted to pair it with SSEs. For example, Shaijumon *et al.* used NVP, NPS and Na as the cathode, electrolyte and anode to assemble a full cell,[114] but the capacity remained at a small value, which is smaller than 40 mAh g^{-1} after 2 cycles. When employing $Na_{2.8}PS_{3.8}Cl_{0.2}$ as electrolytes,[46] the full cell can not only retain its high operating voltage but also increase the discharge capacity. Employing NVP as a cathode can effectively raise the operating voltage of the cell, but the achievable voltage has already approached the upper limit of phosphate-based cathode materials and cannot be further improved. In addition, the NASICON structure of NVP inherently leads to low tap density and low compaction density, which increases the volume fraction of the cathode in the full cell and ultimately reduces the volumetric energy density of the battery. In summary, although the NVP cathode exhibits excellent cycling stability, it is not well suited for high-energy-density battery systems.

6.3 Sulfur and conversion-type cathodes

By observing Table 4, it is not difficult to find that the difference in cathode capacity can be attributed to variations in interfacial compatibility. This phenomenon is particularly pronounced in conversion-type cathodes, especially sulfur cathodes. Sulfur, when employed as a cathode material, offers batteries both high theoretical specific capacity and significant cost benefits, but it is limited by the undesirable shuttle effect of polysulfides.[158–162] SEs serve as a physical barrier to polysulfide ion migration, thereby eradicating the 'shuttle effect' at its source. This capability holds substantial importance for enhancing the cycling longevity of Na/S batteries.[163–165] Tatsumisago's team compared the electrochemical performance of S composites with P_2S_5 and NPS,[122] and the outcomes indicated that a higher specific capacity can be achieved when S is composited with P_2S_5. Skillfully, Zhao's team made use of the self-sacrifice effect in NSS to prepare the S/NSS cathode.[110] An additional capacity can be realized within the combination of NAS and S on the cathode side; thus, the initial capacity can reach 1976 mAh g^{-1}. Even after 140 cycles, the capacity still remained at 1295 mAh g^{-1} without significant capacity decline.

The pre-sodiation of the cathode can effectively mitigate the irreversible capacity loss and stability degradation that exist in alloy anodes during the initial cycling process, and the employment of Na_2S can meet the demand for both a sodium donor and cathode because of its high theoretical capacity and appropriate voltage window. Mitlin *et al.* assembled the full cell with the adoption of a Na_2S cathode, $Na_{2.895}W_{0.3}Sb_{0.7}S_4$ electrolytes and Na–Sn alloy anodes, and the initial capacity was 450 mAh g^{-1}.[152] To improve the inferior electronic and ionic conductivity, Hayasi mixed Na_2S and NaI to prepare solid solution.[153] Compared with bare Na_2S, the ionic conductivity of Na_2S–NaI witnessed a huge enhancement, from 2.5×10^{-13} S cm^{-1} to 1.7×10^{-8} S cm^{-1}. The initial capacity can be further increased to 670 mAh g^{-1} at 0.064 cm^{-2}, which is close to the theoretical capacity of Na_2S (687 mAh g^{-1}). It is noteworthy that Na_2S can be mixed with SSEs to improve the interfacial compatibility. For example, CMK-3 carbon covered with NPS and Na_2S can be realized by the high-temperature melting method, which endows the battery with a capacity of 600 mAh g^{-1} in the first cycle,[115] and increases to 800 mAh g^{-1} during the subsequent operation. Moreover, Jung's team designed a composite cathode by mixing with Na_2S and $Na_{11}Sn_2PS_{12}$ by the liquid-phase method,[154] and the initial capacity can reach 571 mAh g^{-1}, but it is less than that of Na_2S/NPS/CMK-3. This phenomenon could potentially be ascribed to variations in interface compatibility arising from distinct fabrication methods.

Table 4 Different cathode materials for SSEs and their respective parameters

Cathode	Electrolytes	Anode	Rate (mA cm^{-2})	Capacity (mAh g^{-1})/cycles	Average voltage	Ref.
$NaCrO_2$	Na_3PS_4	$Na_{15}Sn_4$	0.013	60/15	2.9 V	87
$NaCrO_2$	Na_3SbS_4	$Na_{15}Sn_4$	0.13	200/20	1.7 V	150
$Na_3V_2(PO_4)_3$	Na_3PS_4	Na	0.02 mA g^{-1}	36/5	3.3 V	114
$Na_3V_2(PO_4)_3$	$Na_{2.8}PS_{3.8}Cl_{0.2}$	Na	10 mA g^{-1}	87/10	3.3 V	46
$S/Na_3PS_{3.85}O_{0.15}$	$Na_3PS_{3.85}O_{0.15}$/ $Na_3PS_{3.4}O_{0.6}$	$Na_{15}Sn_4$	0.13	1200/40	1.5 V	53
S/Na_3PS_4	Na_3PS_4	$Na_{15}Sn_4$	0.127	885/140	1.5 V	110
S/Na_3SbS_4	Na_3SbS_4	$Na_{15}Sn_4$	0.127	1400/140	1.7 V	110
Na_2S	$Na_{2.895}W_{0.3}Sb_{0.7}S_4$	Na_3Sn	0.023	400/10	1.5 V	152
Na_2S–NaI	Na_3PS_4	$Na_{15}Sn_4$	0.038	500/10	1.7 V	153
Na_2S/Na_3PS_4/CMK-3	Na_3PS_4	$Na_{15}Sn_4$	50 mA g^{-1}	800/50	1.5 V	115
$Na_2S/Na_{11}Sn_2PS_{12}$	Na_3PS_4	Na_3Sn	0.3C	200/100	1.8 V	154
FeS_2	Na_3PS_4	Na	60 mA g^{-1}	287/100	1.9 V	155
TiS_2	Na_3PS_4	Na–Sn	0.013	90/10	1.6 V	156
$Ni_{0.7}Fe_{0.3}S_2$	Na_3PS_4	$Na_{15}Sn_4$	0.038	390/30	1.8 V	157
$Co_{0.1}Fe_{0.9}S_2$	$Na_{11}Sn_2SbS_{11.5}Se_{0.5}$/ Na_3PS_4	Na	100 mA g^{-1}	159.8/100	1.7 V	98

Two critical challenges persist: inadequate sulfur utilization stemming from suboptimal solid–solid interfacial contact and sluggish kinetics of sulfur redox reactions. The superior ionic conductivity of SSEs has effectively ameliorated the kinetic limitations of cathodic S. Nonetheless, inadequate interfacial contact still remains a challenge that necessitates optimization *via* modifications to both cathode materials and electrolyte formulations. Mechanical mixing of SSEs or other materials (sulfides, halides, *etcl.*) with S has a positive role in regulating the interface compatibility. To achieve high energy density at the same weight, conversion-type cathode materials exhibiting multi-electron transfer effects have garnered extensive research interest. Typical conversion-type cathodes, such as FeS_2 (ref. 155) and TiS_2 (ref. 156), have been successfully introduced to couple with NSP SSEs. Hayashi's team modified FeS_2 with Ni elements.[157] The introduction of Ni helps to improve the discharge capacity of the cathode, which can reach 390 mAh g^{-1} and remain stable after cycling 30 times. Similarly, Yao *et al.* further added cobalt element into FeS_2 to prepare $Co_{0.1}Fe_{0.9}S_2$.[98] The full cell can retain a high capacity of 159.8 mAh g^{-1} after operating for 100 cycles at a high current density of 100 mA g^{-1}.

Sulfur cathodes (or other conversion-type cathodes) paired with metal or alloy anodes are widely regarded as a promising route to achieve high-energy-density SSE-SMBs with energy density exceeding 500 Wh kg^{-1}, and this combination can effectively suppress issues such as dendrite growth, the shuttle effect and polysulfide dissolution. However, the low electronic and ionic conductivity of elemental sulfur and its discharge by-product (Na_2S) leads to slow reaction kinetics and poor interfacial compatibility, which severely limits the overall reaction kinetics and the utilization rate of active materials. Furthermore, large volume fluctuation of sulfur during cycling further reduces the relative content of active materials in the electrode. As a result, SSE-SMBs constructed with high-capacity cathodes often suffer from significant degradation of cycling stability within a short cycling period.

7 Conclusion and perspectives

In conclusion, SSEs are known for their outstanding ionic conductivity and plasticity and are regarded as promising candidates for ASSMBs. This review briefly illustrated the crystal structure, ion transport mechanism, critical challenges and related modification strategies. Next, the scalable preparation of electrode materials was mentioned. Finally, we discussed the application of SSEs in diverse cathode systems. These discussions aim to provide design guidance for high energy density SSE-SMBs.

(1) From the perspective of the cathode, high energy density implies that the cathode should be equipped with a high capacity and a high voltage plateau. The selection of S or transfer-type cathodes can well meet the demand of high capacity, and the design of high valence S in anode-free Na/S batteries can achieve the highest energy density (2021 Wh kg^{-1}),[166] while enhancing battery safety by the abandonment of metallic Na. As an electronic insulator, the ion transport of cathodic S completely relies on the external conductive network, and the stress generated by the volume change during the cycling process will damage the transport network, leading to the decline in cycling stability. In the absence of electrolyte assistance, the deactivation phenomenon of the S cathode in SSE-SMBs becomes even more rigorous. The strategies such as cathode coating, integrated cathodes and composite cathodes have been adopted. The interface coating can stabilize the interface, suppress the harmful side reactions, and simultaneously reduce the interface resistance for ion transport from the cathode to the SSEs. The incorporation of composite cathode serves to convert the pre-existing "point contact" into a continuous ion-conducting network. This transformation effectively maximizes both the solid–solid contact area and the ion transport area, which is significance for reducing the interfacial impedance. The design of integrated cathodes can significantly reduce the number of macroscopic interfaces, simplify the battery assembly process, and improve the

volumetric energy density. When pursuing high energy density, the loading of the active material should be as high as possible, while the proportion of non-active materials should be as low as possible. However, this change eventually damages the utilization of S, which means that the above modification methods cannot fully meet the need for high S loading. The balance between a high loading cathode and interfacial compatibility warrants in-depth investigation.

(2) At the electrolyte level, SEs should balance a wide electrochemical window with a thin thickness to pursuit high energy density. Currently, the electrochemical windows of most SSEs are less than 3 V, and excessively high voltage can lead to cathodic oxidation and anodic reduction. Therefore, the development of SSEs that can remain stable at high voltages cannot be overlooked. SEs with high mechanical strength play a positive role in suppressing dendrite expansion, but SSEs cannot effectively restrict the growth of dendrites because of the excellent processability, and this issue will be magnified when SSEs become thinner. In addition, the design of thin SSEs also multiples the challenge of fast charging. Therefore, it is necessary to enhance the inherent mechanical strength of SSEs through densification or modification (doping or replacing).

(3) The application of anode-less and anode-free SMBs can reduce the weight of the anode and simplify the manufacturing process,[167,168] thereby demonstrating high energy density and low manufacturing cost. However, Na provided by the cathode side during the initial charging process is the main source and cannot be supplemented by other ways, and the Na loss caused by the side reactions will lead to irreversible capacity loss. Therefore, the ionic conductivity, interface stability and mechanical strength of SSEs should be improved. This is because the outstanding interface stability can stabilize the interface between SSEs and highly reactive metal anodes without side reactions. The enhancement of mechanical strength can withstand the stress generated by volume changes and restrain dendrite propagation. Finally, high ionic conductivity of SSEs is beneficial for boosting ion diffusion, and uniform sodium deposition can be realized, which eventually enhances the durability of SSE-SMBs.

Author contributions

Kaizhi Chen and Haohua Jiang: investigation, data curation and writing original draft. Hongyu Li, Xianglong Huang, Kunjie Zhu and Long Yao: review and editing. Weihong Lai and Yunxiao Wang: conceptualization, supervision, funding acquisition, and review and editing.

Conflicts of interest

There are no conflicts to declare.

Data availability

No primary research results, software or code have been included and no new data were generated or analysed as part of this review.

Acknowledgements

This work was supported by the National Natural Science Foundation of China (No. 22579113, 52350710795, 22579113, 22509130, and 52501285) and the Science and Technology Commission of Shanghai Municipality (No. 24ZR1454500).

References

1 H. Wang, E. Matios, J. Luo and W. Li, *Chem. Soc. Rev.*, 2020, **49**, 3783–3805.
2 T. Perveen, M. Siddiq, N. Shahzad, R. Ihsan, A. Ahmad and M. I. Shahzad, *Renewable Sustainable Energy Rev.*, 2020, **119**, 109549.
3 M. Li, J. Lu, Z. Chen and K. Amine, *Adv. Mater.*, 2018, **30**, 1800561.
4 L. Zhao, Y. Tao, Y. Zhang, Y. Lei, W.-H. Lai, S. Chou, H.-K. Liu, S.-X. Dou and Y.-X. Wang, *Adv. Mater.*, 2024, **36**, 2402337.
5 Z. Yang, J. Zhang, M. C. W. Kintner-Meyer, X. Lu, D. Choi, J. P. Lemmon and J. Liu, *Chem. Rev.*, 2011, **111**, 3577–3613.
6 J.-Y. Hwang, S.-T. Myung and Y.-K. Sun, *Chem. Soc. Rev.*, 2017, **46**, 3529–3614.
7 Y. Liu, X. Liu, G. Zhang, X. Shi, P. Zhang, Y. Fan, Y. Huang and R. Zhang, *ACS Appl. Mater. Interfaces*, 2023, **15**(22), 26691–26699.
8 W. Luo and L. Hu, *ACS Cent. Sci.*, 2015, **1**, 420–422.
9 K. Chen, X. Xia, H. Ma, S. Xu, Y. Yao, X. Rui and Y. Yu, *Energy Mater. Adv.*, 2023, **4**, 0063.
10 Z. W. Seh, J. Sun, Y. Sun and Y. Cui, *ACS Cent. Sci.*, 2015, **1**, 449–455.
11 E. Goikolea, V. Palomares, S. Wang, I. R. de Larramendi, X. Guo, G. Wang and T. Rojo, *Adv. Energy Mater.*, 2020, **10**, 2002055.
12 X. Zheng, L. Huang, X. Ye, J. Zhang, F. Min, W. Luo and Y. Huang, *Chem*, 2021, **7**, 2312–2346.
13 D. Ruiz-Martínez, A. Kovacs and R. Gómez, *Energy Environ. Sci.*, 2017, **10**, 1936–1941.
14 S. Sarkar, M. J. Lefler, B. S. Vishnugopi, R. B. Nuwayhid, C. T. Love, R. Carter and P. P. Mukherjee, *Cell Rep. Phys. Sci.*, 2023, **4**, 101356.
15 J. Zheng, S. Chen, W. Zhao, J. Song, M. H. Engelhard and J.-G. Zhang, *ACS Energy Lett.*, 2018, **3**, 315–321.
16 J. Ma, M. Wang, H. Zhang, Z. Shang, L. Fu, W. Zhang, B. Song and K. Lu, *Adv. Funct. Mater.*, 2023, **33**, 2214430.
17 X. Wang, R. Kerr, F. Chen, N. Goujon, J. M. Pringle, D. Mecerreyes, M. Forsyth and P. C. Howlett, *Adv. Mater.*, 2020, **32**, 1905219.
18 Y. Qiu and J. Xu, *Nano Res.*, 2024, **17**, 1402–1426.
19 H. Gao, S. Xin, L. Xue and J. B. Goodenough, *Chem*, 2018, **4**, 833–844.
20 Q. Liu, Z. Geng, C. Han, Y. Fu, S. Li, Y. He, F. Kang and B. Li, *J. Power Sources*, 2018, **389**, 120–134.
21 Y. Su, L. Ye, W. Fitzhugh, Y. Wang, E. Gil-González, I. Kim and X. Li, *Energy Environ. Sci.*, 2020, **13**, 908–916.
22 X.-B. Cheng, R. Zhang, C.-Z. Zhao and Q. Zhang, *Chem. Rev.*, 2017, **117**, 10403–10473.

23 Q. Zhang, D. Cao, Y. Ma, A. Natan, P. Aurora and H. Zhu, *Adv. Mater.*, 2019, **31**, 1901131.
24 Y. Deng, J. Chen, Y. Yue, C. Liu, M. Cui, Q. Xiang, H. Zhao, Z. Cao, K. Jia, L. Jin, Y. Li, Y. Liu, J. Wang, G. Feng and K. Xi, *Carbon Neutralization*, 2025, **4**, e70037.
25 L. Shan, B. Chen, Y. Hu, X. Gan, H. Si, Y. Wang, Z. Chen, Y. Zhang, Y. Zhou, L. Ding and J. Ding, *Aggregate*, 2025, **6**, e70117.
26 X. Wang, J. Li, Z. Hu, X. Li, L. Liu, J. Wang, J. H. Kim, W. Li, W. K. Pang and B. Johannessen, *Adv. Sci.*, 2025, **12**, e15463.
27 L. Zhou, S. Zhang, W. Li, B. Li, N. S. Grundish, P. Ren, X. Wang, N. Wu, W. Zhou and Y. Li, *J. Am. Chem. Soc.*, 2025, **147**, 15136–15145.
28 M. Wu, X. Qi, P. Lei, W. Ren, Y. Li, H. Liu, J. Zeng, L. Gao, C.-W. Nan and L.-Z. Fan, *ACS Nano*, 2025, **19**, 35740–35751.
29 M. Wu, X. Liu, H. Liu, D. Li, X. Qi, J. Zeng, L. Gao, C.-W. Nan and L.-Z. Fan, *Nat. Commun.*, 2025, **16**, 2808.
30 S. Liu, L. Zhou and K. Neyts, *Adv. Energy Mater.*, 2025, **16**(4), e05286.
31 Y. Li, X. Tang, Q. Li, Y.-X. Yin, L. Liu, J. Zhao and Y.-S. Hu, *ACS Energy Lett.*, 2025, **10**, 5520–5541.
32 Q. Yu, J. Hu, Y. Xu, R. Cao, S. Chen and C. Li, *Angew. Chem., Int. Ed.*, 2025, **64**, e202425503.
33 Y. Guo, K. Liu, C. Li, D. Song, H. Zhang, Z. Wang, Y. Yan, L. Zhang and S. Dai, *Adv. Energy Mater.*, 2024, **14**, 2401504.
34 P. Lu, D. Wu, L. Chen, H. Li and F. Wu, *Electrochem. Energy Rev.*, 2022, **5**, 3.
35 Y. Nikodimos, C.-J. Huang, B. W. Taklu, W.-N. Su and B. J. Hwang, *Energy Environ. Sci.*, 2022, **15**, 991–1033.
36 A. Banerjee, K. H. Park, J. W. Heo, Y. J. Nam, C. K. Moon, S. M. Oh, S.-T. Hong and Y. S. Jung, *Angew. Chem., Int. Ed.*, 2016, **55**, 9634–9638.
37 Z. Zhang, E. Ramos, F. Lalère, A. Assoud, K. Kaup, P. Hartman and L. F. Nazar, *Energy Environ. Sci.*, 2018, **11**, 87–93.
38 Z. Yu, S.-L. Shang, J.-H. Seo, D. Wang, X. Luo, Q. Huang, S. Chen, J. Lu, X. Li, Z.-K. Liu and D. Wang, *Adv. Mater.*, 2017, **29**, 1605561.
39 L. Yu, J. Yin, C. Gao, C. Lin, X. Shen, S. Dai and Q. Jiao, *ACS Appl. Mater. Interfaces*, 2023, **15**, 31635–31642.
40 F. Tsuji, A. Nasu, C. Hotehama, A. Sakuda, M. Tatsumisago and A. Hayashi, *Mater. Adv.*, 2021, **2**, 1676–1682.
41 S. Harm, A.-K. Hatz, C. Schneider, C. Hoefer, C. Hoch and B. V. Lotsch, *Front. Chem.*, 2020, **8**, 2296–2646.
42 A. Hayashi, *Electrochemistry*, 2023, **91**, 101002.
43 L. Gao, G. Bian, Y. Yang, B. Zhang, X. Wu and K. Wu, *New J. Chem.*, 2021, **45**, 12362–12366.
44 L. Zhang, K. Yang, J. Mi, L. Lu, L. Zhao, L. Wang, Y. Li and H. Zeng, *Adv. Energy Mater.*, 2015, **5**, 1501294.
45 F. Tsuji, A. Nasu, A. Sakuda, M. Tatsumisago and A. Hayashi, *J. Power Sources*, 2021, **506**, 230100.
46 X. Feng, P.-H. Chien, Z. Zhu, I.-H. Chu, P. Wang, M. Immediato-Scuotto, H. Arabzadeh, S. P. Ong and Y.-Y. Hu, *Adv. Funct. Mater.*, 2019, **29**, 1807951.
47 F. Tsuji, N. Masuzawa, A. Sakuda, M. Tatsumisago and A. Hayashi, *ACS Appl. Energy Mater.*, 2020, **3**, 11706–11712.
48 A. Hayashi, N. Masuzawa, S. Yubuchi, F. Tsuji, C. Hotehama, A. Sakuda and M. Tatsumisago, *Nat. Commun.*, 2019, **10**, 5266.
49 T. Takayanagi, A. Nasu, F. Tsuji, K. Motohashi, A. Sakuda, M. Tatsumisago and A. Hayashi, *J. Ceram. Soc. Jpn.*, 2022, **130**, 498–503.
50 L. Shu, C. Gao, Y. Liu, X. Zhou, H. Ma, X. Zhang, X. Shen, S. Dai, C. Lin and Q. Jiao, *J. Colloid Interface Sci.*, 2023, **652**, 2042–2053.
51 H. Jia, Y. Sun, Z. Zhang, L. Peng, T. An and J. Xie, *Energy Storage Mater.*, 2019, **23**, 508–513.
52 L. Yu, Q. Jiao, B. Liang, H. Shan, C. Lin, C. Gao, X. Shen and S. Dai, *J. Alloys Compd.*, 2022, **913**, 165229.
53 X. Chi, Y. Zhang, F. Hao, S. Kmiec, H. Dong, R. Xu, K. Zhao, Q. Ai, T. Terlier, L. Wang, L. Zhao, L. Guo, J. Lou, H. L. Xin, S. W. Martin and Y. Yao, *Nat. Commun.*, 2022, **13**, 2854.
54 S. Xiong, Z. Liu, L. Yang, Y. Ma, W. Xu, J. Bai and H. Chen, *Mater. Today Phys.*, 2020, **15**, 100281.
55 S. Han, J. Y. Seo, W. B. Park, A. B. Ikhe, S. Y. Choi, S. C. Han, K.-S. Sohn and M. Pyo, *J. Mater. Chem. A*, 2022, **10**, 25039–25046.
56 A. Ponrouch, E. Marchante, M. Courty, J.-M. Tarascon and M. R. Palacín, *Energy Environ. Sci.*, 2012, **5**, 8572–8583.
57 W. D. Richards, T. Tsujimura, L. J. Miara, Y. Wang, J. C. Kim, S. P. Ong, I. Uechi, N. Suzuki and G. Ceder, *Nat. Commun.*, 2016, **7**, 11009.
58 Z. Yu, S.-L. Shang, Y. Gao, D. Wang, X. Li, Z.-K. Liu and D. Wang, *Nano Energy*, 2018, **47**, 325–330.
59 Z. Zhang, E. Ramos, F. Lalère, A. Assoud, K. Kaup, P. Hartman and L. F. Nazar, *Energy Environ. Sci.*, 2018, **11**, 87–93.
60 G. Liu, X. Sun, X. Yu, W. Weng, J. Yang, D. Zhou, R. Xiao, L. Chen and X. Yao, *Chem. Eng. J.*, 2021, **420**, 127692.
61 A. Tiwari, S. K. Singh, N. Srivastava, D. Meghnani, R. Mishra, R. K. Tiwari, A. Patel, H. Gupta, V. K. Tiwari and R. K. Singh, *J. Phys. D: Appl. Phys.*, 2022, **55**, 355503.
62 E. P. Ramos, A. Assoud, L. Zhou, A. Shyamsunder, D. Rettenwander and L. F. Nazar, *APL Mater.*, 2023, **11**, 011104.
63 W. Weng, G. Liu, L. Shen and X. Yao, *J. Power Sources*, 2021, **512**, 230485.
64 L. Zhang, D. Zhang, K. Yang, X. Yan, L. Wang, J. Mi, B. Xu and Y. Li, *Adv. Sci.*, 2016, **3**, 1600089.
65 S. Nishimura, A. Hayashi, A. Sakuda and A. Yamada, *ACS Appl. Energy Mater.*, 2022, **5**, 14053–14058.
66 J. Huang, K. Wu, G. Xu, M. Wu, S. Dou and C. Wu, *Chem. Soc. Rev.*, 2023, **52**, 4933–4995.
67 M. S. Nafis, Z. Liang, S. Lee and C. Ban, *Nano Energy*, 2025, **133**, 110447.
68 P. Till, M. T. Agne, M. A. Kraft, M. Courty, T. Famprikis, M. Ghidiu, T. Krauskopf, C. Masquelier and W. G. Zeier, *Chem. Mater.*, 2022, **34**, 2410–2421.
69 D. Ren, L. Lu, R. Hua, G. Zhu, X. Liu, Y. Mao, X. Rui, S. Wang, B. Zhao, H. Cui, M. Yang, H. Shen, C.-Z. Zhao, L. Wang, X. He, S. Liu, Y. Hou, T. Tan, P. Wang, Y. Nitta and M. Ouyang, *eTransportation*, 2023, **18**, 100272.

70 L. Hu, J. Wang, K. Wang, Z. Gu, Z. Xi, H. Li, F. Chen, Y. Wang, Z. Li and C. Ma, *Nat. Commun.*, 2023, **14**, 3807.
71 F. Schnaubelt, A. Panda, D. Wagner, M. Ziegler, H. A. Dang, W. G. Zeier, A. Bielefeld and J. Janek, *Adv. Energy Mater.*, 2025, **15**, e03047.
72 O. Maus, M. A. Lange, F. Frankenberg, F. Stainer, V. Faka, E. Schlautmann, C. Rosenbach, A. Jodlbauer, J. Schubert, J. Janek, C. Li, P. Michalowski, H. M. R. Wilkening, A. Kwade and W. G. Zeier, *Adv. Energy Mater.*, 2025, **15**, 2403291.
73 Z. Guo, Q. Zhu, T. Chen, J. Sun, L. Bai, Y. Liu, H. Niu, Y. He, F. Yu, K. Liu, C. Liu, J. Xu, S. Li and Z. Chang, *ACS Nano*, 2025, **19**, 26347–26363.
74 C. Yu, S. Ganapathy, N. J. J. de Klerk, E. R. H. van Eck and M. Wagemaker, *J. Mater. Chem. A*, 2016, **4**, 15095–15105.
75 X. Feng, H. Fang, N. Wu, P. Liu, P. Jena, J. Nanda and D. Mitlin, *Joule*, 2022, **6**, 543–587.
76 T. Famprikis, J. A. Dawson, F. Fauth, O. Clemens, E. Suard, B. Fleutot, M. Courty, J.-N. Chotard, M. S. Islam and C. Masquelier, *ACS Mater. Lett.*, 2019, **1**, 641–646.
77 J. Lin, M. Schaller, G. Cherkashinin, S. Indris, J. Du, C. Ritter, A. Kondrakov, J. Janek, T. Brezesinski and F. Strauss, *Small*, 2024, **20**, 2306832.
78 M. Yang, L. Chen, H. Li and F. Wu, *Energy Mater. Adv.*, 2022, **2022**, 0041.
79 G. Li, H. Zheng, Y. Yang, D. Zhao, Y. Shen, J. Chen, S. Wu, H. Zhu, Y. Yang, H. Liu and H. Duan, *ACS Energy Lett.*, 2025, 2600–2609.
80 J. Xu, Y. Li, P. Lu, W. Yan, M. Yang, H. Li, L. Chen and F. Wu, *Adv. Energy Mater.*, 2022, **12**, 2102348.
81 H. Tsukasaki, H. Sano, K. Igarashi, A. Wakui, T. Yaguchi and S. Mori, *J. Power Sources*, 2022, **524**, 231085.
82 Y. Tian, T. Shi, W. D. Richards, J. Li, J. C. Kim, S.-H. Bo and G. Ceder, *Energy Environ. Sci.*, 2017, **10**, 1150–1166.
83 H. Tang, Z. Deng, Z. Lin, Z. Wang, I.-H. Chu, C. Chen, Z. Zhu, C. Zheng and S. P. Ong, *Chem. Mater.*, 2018, **30**, 163–173.
84 J. Haruyama, K. Sodeyama, L. Han, K. Takada and Y. Tateyama, *Chem. Mater.*, 2014, **26**, 4248–4255.
85 Y. Li, G. Liu, J. Che, L. Chen, X. Wang, G. Wang, L. Lei, J. Hou, S. Li, J. Wang, Y. Xu and Y. Zhao, *Interdiscip. Mater.*, 2025, **4**, 24–51.
86 Z. Xu, X. Wang, Z. Wang, X. Li, J. Liu, A. Bayaguud and L. Zhang, *J. Power Sources*, 2023, **571**, 233079.
87 A. Hayashi, K. Noi, N. Tanibata, M. Nagao and M. Tatsumisago, *J. Power Sources*, 2014, **258**, 420–423.
88 P. Minnmann, F. Strauss, A. Bielefeld, R. Ruess, P. Adelhelm, S. Burkhardt, S. L. Dreyer, E. Trevisanello, H. Ehrenberg, T. Brezesinski, F. H. Richter and J. Janek, *Adv. Energy Mater.*, 2022, **12**, 2201425.
89 J. Fu, C. Wang, S. Wang, J. W. Reid, J. Liang, J. Luo, J. T. Kim, Y. Zhao, X. Yang, F. Zhao, W. Li, B. Fu, X. Lin, Y. Hu, H. Su, X. Hao, Y. Gao, S. Zhang, Z. Wang, J. Liu, H. Abdolvand, T.-K. Sham, Y. Mo and X. Sun, *Nature*, 2025, 1–8.
90 B. Liang, G. Wang, H. Shan, P. Dong, L. Yu, C. Lin, C. Gao, Y. Liu, X. Shen and Q. Jiao, *J. Am. Ceram. Soc.*, 2023, **106**, 3199–3208.
91 R. P. Rao, H. Chen, L. L. Wong and S. Adams, *J. Mater. Chem. A*, 2017, **5**, 3377–3388.
92 M. Lazar, S. Kmiec, A. Joyce and S. W. Martin, *ACS Appl. Energy Mater.*, 2020, **3**, 11559–11569.
93 L. E. Goodwin, P. Till, M. Bhardwaj, N. Nazer, P. Adelhelm, F. Tietz, W. G. Zeier, F. H. Richter and J. Janek, *ACS Appl. Mater. Interfaces*, 2023, **15**, 50457–50468.
94 K. Noi, Y. Nagata, T. Hakari, K. Suzuki, S. Yubuchi, Y. Ito, A. Sakuda, A. Hayashi and M. Tatsumisago, *ACS Appl. Mater. Interfaces*, 2018, **10**, 19605–19614.
95 L. Li, R. Xu, L. Zhang, Z. Zhang, M. Yang, D. Liu, X. Yan and A. Zhou, *Adv. Funct. Mater.*, 2022, **32**, 2203095.
96 N. Tanibata, K. Noi, A. Hayashi and M. Tatsumisago, *RSC Adv.*, 2014, **4**, 17120–17123.
97 Z. Yu, S.-L. Shang, Y. Gao, D. Wang, X. Li, Z.-K. Liu and D. Wang, *Nano Energy*, 2018, **47**, 325–330.
98 H. Wan, L. Cai, W. Weng, J. P. Mwizerwa, J. Yang and X. Yao, *J. Power Sources*, 2020, **449**, 227515.
99 Z. Yu, S.-L. Shang, D. Wang, Y. C. Li, H. P. Yennawar, G. Li, H.-T. Huang, Y. Gao, T. E. Mallouk, Z.-K. Liu and D. Wang, *Energy Storage Mater.*, 2019, **17**, 70–77.
100 Y. Feng, J. Liu, Z. Wei, S. Yao, G. Chen and F. Du, *Angew. Chem., Int. Ed.*, 2025, **64**, e202507247.
101 P. Hu, Y. Zhang, X. Chi, K. Kumar Rao, F. Hao, H. Dong, F. Guo, Y. Ren, L. C. Grabow and Y. Yao, *ACS Appl. Mater. Interfaces*, 2019, **11**, 9672–9678.
102 Y. Li, W. Arnold, S. Halacoglu, J. B. Jasinski, T. Druffel and H. Wang, *Adv. Funct. Mater.*, 2021, **31**, 2101636.
103 M. Mwemezi, W. B. Park and A. B. Ikhe, *Electrochim. Acta*, 2024, **480**, 143919.
104 W. Liu, P. Liu and D. Mitlin, *Adv. Energy Mater.*, 2020, **10**, 2002297.
105 C. Bao, B. Wang, P. Liu, H. Wu, Y. Zhou, D. Wang, H. Liu and S. Dou, *Adv. Funct. Mater.*, 2020, **30**, 2004891.
106 T. Wang, Y. Hua, Z. Xu and J. S. Yu, *Small*, 2022, **18**, 2102250.
107 S. Wenzel, T. Leichtweiss, D. A. Weber, J. Sann, W. G. Zeier and J. Janek, *ACS Appl. Mater. Interfaces*, 2016, **8**, 28216–28224.
108 S. Zhang, Y. Zhao, F. Zhao, L. Zhang, C. Wang, X. Li, J. Liang, W. Li, Q. Sun, C. Yu, J. Luo, K. Doyle-Davis, R. Li, T.-K. Sham and X. Sun, *Adv. Funct. Mater.*, 2020, **30**, 2001118.
109 X. Hu, M. Wang, Y. Liu, X. Meng, Y. Zhong, X. Wang and J. Tu, *Chem. Eng. J.*, 2024, **499**, 156290.
110 Y. Yuan, Y. Hu, Y. Gan, Z. L. Dong, Y. Wang, E. Jin, M. Yang, F. B. Holness, V. Martins, Q. Tu and Y. Zhao, *Energy Environ. Sci.*, 2025, **18**, 4288–4301.
111 Y. Tian, Y. Sun, D. C. Hannah, Y. Xiao, H. Liu, K. W. Chapman, S.-H. Bo and G. Ceder, *Joule*, 2019, **3**, 1037–1050.
112 Y. Huang, M. Xie, J. Zhang, Z. Wang, Y. Jiang, G. Xiao, S. Li, L. Li, F. Wu and R. Chen, *Nano Energy*, 2017, **39**, 273–283.

113 J. Wang, C. Yang, S. Chen, Y. Wu, X. Sun, C. Huang, R. Tang, J. Ke, Y. Dai, Y. Situ and H. Huang, *J. Alloys Compd.*, 2023, **938**, 168350.
114 P. Aswathy, S. Suriyakumar, S. A. Kumar, M. S. Oliyantakath Hassan, V. Vijayan and M. M. Shaijumon, *ACS Appl. Energy Mater.*, 2022, **5**, 12592–12601.
115 X. Fan, J. Yue, F. Han, J. Chen, T. Deng, X. Zhou, S. Hou and C. Wang, *ACS Nano*, 2018, **12**, 3360–3368.
116 T. Ando, A. Sakuda, M. Tatsumisago and A. Hayashi, *Electrochem. Commun.*, 2020, **116**, 106741.
117 J. Yue, X. Zhu, F. Han, X. Fan, L. Wang, J. Yang and C. Wang, *ACS Appl. Mater. Interfaces*, 2018, **10**, 39645–39650.
118 H. Wan, J. P. Mwizerwa, X. Qi, X. Liu, X. Xu, H. Li, Y.-S. Hu and X. Yao, *ACS Nano*, 2018, **12**, 2809–2817.
119 E. A. Wu, S. Banerjee, H. Tang, P. M. Richardson, J.-M. Doux, J. Qi, Z. Zhu, A. Grenier, Y. Li, E. Zhao, G. Deysher, E. Sebti, H. Nguyen, R. Stephens, G. Verbist, K. W. Chapman, R. J. Clément, A. Banerjee, Y. S. Meng and S. P. Ong, *Nat. Commun.*, 2021, **12**, 1256.
120 H. Xu, X. Lin, H. Chang, P. Apostol, J. Wang, X. Liu, X. Zhang, D. Tie and A. Vlad, *Chin. J. Chem.*, 2026, **44**, 73–79.
121 Z.-W. Wang, J.-D. Luo, Z.-Y. Huang, W. Li, H.-Y. Tan, X. Cheng, M.-Y. Zhou, X.-D. Hao, C.-P. Luo, C. Wan, L. Wang, Y.-C. Yin, S. Jiao and H.-B. Yao, *J. Am. Chem. Soc.*, 2025, **147**, 35283–35292.
122 N. Tanibata, H. Tsukasaki, M. Deguchi, S. Mori, A. Hayashi and M. Tatsumisago, *Solid State Ionics*, 2017, **311**, 6–13.
123 A. Nasu, A. Sakuda, M. Tatsumisago and A. Hayashi, *J. Ceram. Soc. Jpn.*, 2022, **130**, 789–793.
124 A. Nasu, M. Otoyama, A. Sakuda, A. Hayashi and M. Tatsumisago, *J. Ceram. Soc. Jpn.*, 2019, **127**, 514–517.
125 A. Nasu, A. Sakuda, T. Kimura, M. Deguchi, A. Tsuchimoto, M. Okubo, A. Yamada, M. Tatsumisago and A. Hayashi, *Small*, 2022, **18**, 2203383.
126 A. Nasu, A. Sakuda, M. Tatsumisago and A. Hayashi, *J. Ceram. Soc. Jpn.*, 2022, **130**, 789–793.
127 A. Nasu, M. Otoyama, A. Sakuda, A. Hayashi and M. Tatsumisago, *J. Ceram. Soc. Jpn.*, 2019, **127**, 514–517.
128 A. Nasu, A. Sakuda, T. Kimura, M. Deguchi, A. Tsuchimoto, M. Okubo, A. Yamada, M. Tatsumisago and A. Hayashi, *Small*, 2022, **18**, 2203383.
129 Z.-W. Wang, J.-D. Luo, Z.-Y. Huang, W. Li, H.-Y. Tan, X. Cheng, M.-Y. Zhou, X.-D. Hao, C.-P. Luo, C. Wan, L. Wang, Y.-C. Yin, S. Jiao and H.-B. Yao, *J. Am. Chem. Soc.*, 2025, **147**, 35283–35292.
130 P. Lu, L. Liu, S. Wang, J. Xu, J. Peng, W. Yan, Q. Wang, H. Li, L. Chen and F. Wu, *Adv. Mater.*, 2021, **33**, 2100921.
131 S. Yubuchi, A. Hayashi and M. Tatsumisago, *Chem. Lett.*, 2015, **44**, 884–886.
132 M. Atsunori, H. Gamo and N. H. H. Phuc, *Heliyon*, 2019, **5**, e02760.
133 M. Uematsu, S. Yubuchi, K. Noi, A. Sakuda, A. Hayashi and M. Tatsumisago, *Solid State Ionics*, 2018, **320**, 33–37.
134 X. Zuo, K. Chang, J. Zhao, Z. Xie, H. Tang, B. Li and Z. Chang, *J. Mater. Chem. A*, 2016, **4**, 51–58.
135 A. Banerjee, K. H. Park, J. W. Heo, Y. J. Nam, C. K. Moon, S. M. Oh, S.-T. Hong and Y. S. Jung, *Angew. Chem.*, 2016, **128**, 9786–9790.
136 Y. Li, J. Chen, P. Cai and Z. Wen, *J. Mater. Chem. A*, 2018, **6**, 4948–4954.
137 Z. Zhang, L. Wu, D. Zhou, W. Weng and X. Yao, *Nano Lett.*, 2021, **21**, 5233–5239.
138 X. Miao, Y. Wu, H. Jing, Y. Cao, Y. Wang, J. Moon and X. Li, *Energy Environ. Sci.*, 2025, **18**, 8197–8208.
139 M. Tang, S. Dong, K. Yue, J. Zhao, W. Li, X. Wang, P. Chen, R. Liu, R. Wen, S. Song, Y. Liu, J. Nai, J. Wang, Q. Zhu, L. Cheng, H. Lan, L. Wu, B. Zhou, D. Yang, X. Tao, L. Guo and H. Wang, *Nat. Synth.*, 2025, 11.
140 S. Kawaguchi, H. Tanaka, N. Fukiya, K. Ehara, Y. Sasaki, M. Kuzuhara and T. Miyuki, *Adv. Mater.*, 2025, e17806.
141 R. Li, N. Chen, S. Liu, Y. Mao, Z. Liao, K. Qiu, P. Wang, T. Zhang, S. Hao, G. Zhu, C. Guo, X. Liu, D. Ren, L. Lu and M. Ouyang, *Adv. Funct. Mater.*, 2024, **34**, 2409403.
142 L. Zhu, D. Wu, C. Guo, J. Peng, Z. Jiang, G. Ma, C. Xu, W. He, L. Chen and F. Wu, *Energy Storage Mater.*, 2025, **79**, 104338.
143 H. Tsukasaki, M. Otoyama, Y. Mori, S. Mori, H. Morimoto, A. Hayashi and M. Tatsumisago, *J. Power Sources*, 2017, **367**, 42–48.
144 H. Chung and B. Kang, *Chem. Mater.*, 2017, **29**, 8611–8619.
145 J. Yan, J. Yao, J. Zhao, Z. Yu, Z. Ye, L. Zhang, Z. Wang, X. Zhang, Z. Rong, D. Kong, J. Sun, W. Li, J. Wang, D. Gao, J. Huang and Y. Tang, *Adv. Funct. Mater.*, 2025, **35**(25), 2421918.
146 R. Chen, A. M. Nolan, J. Lu, J. Wang, X. Yu, Y. Mo, L. Chen, X. Huang and H. Li, *Joule*, 2020, **4**, 812–821.
147 S. Wang, Y. Wu, T. Ma, L. Chen, H. Li and F. Wu, *ACS Nano*, 2022, **16**, 16158–16176.
148 D. L. R. Melvin, M. Siniscalchi, D. Spencer-Jolly, B. Hu, Z. Ning, S. Zhang, J. Bu, S. Marathe, A. Bonnin, J. Ihli, G. J. Rees, P. S. Grant, C. W. Monroe, T. J. Marrow, G. Li and P. G. Bruce, *Nat. Energy*, 2025, **10**, 1205–1214.
149 H. Du, X. Zhang and H. Yu, *eTransportation*, 2025, **23**, 100382.
150 D. Zhang, X. Cao, D. Xu, N. Wang, C. Yu, W. Hu, X. Yan, J. Mi, B. Wen, L. Wang and L. Zhang, *Electrochim. Acta*, 2018, **259**, 100–109.
151 Z. Gu, J. Ma, F. Zhu, T. Liu, K. Wang, C.-W. Nan, Z. Li and C. Ma, *Nat. Commun.*, 2023, **14**, 1632.
152 X. Feng, H. Fang, P. Liu, N. Wu, E. C. Self, L. Yin, P. Wang, X. Li, P. Jena, J. Nanda and D. Mitlin, *Angew. Chem., Int. Ed.*, 2021, **60**, 26158–26166.
153 Y. Fujita, A. Nasu, A. Sakuda, M. Tatsumisago and A. Hayashi, *J. Power Sources*, 2022, **532**, 231313.
154 J. E. Lee, K.-H. Park, J. C. Kim, T.-U. Wi, A. R. Ha, Y. B. Song, D. Y. Oh, J. Woo, S. H. Kweon, S. J. Yeom, W. Cho, K. Kim, H.-W. Lee, S. K. Kwak and Y. S. Jung, *Adv. Mater.*, 2022, **34**, 2200083.
155 H. Wan, J. P. Mwizerwa, X. Qi, X. Xu, H. Li, Q. Zhang, L. Cai, Y.-S. Hu and X. Yao, *ACS Appl. Mater. Interfaces*, 2018, **10**, 12300–12304.

156 A. Nasu, T. Inaoka, F. Tsuji, K. Motohashi, A. Sakuda, M. Tatsumisago and A. Hayashi, *ACS Appl. Mater. Interfaces*, 2022, **14**, 24480–24485.
157 G. Shirota, A. Nasu, A. Sakuda, M. Deguchi, K. Motohashi, M. Tatsumisago and A. Hayashi, *Electrochemistry*, 2022, **90**, 37011.
158 Y.-J. Lei, X. Lu, H. Yoshikawa, D. Matsumura, Y. Fan, L. Zhao, J. Li, S. Wang, Q. Gu, H.-K. Liu, S.-X. Dou, S. Devaraj, T. Rojo, W.-H. Lai, M. Armand, Y.-X. Wang and G. Wang, *Nat. Commun.*, 2024, **15**, 3325.
159 X.-L. Huang, X. Li, L. Zhao, L. Yao, K. Zhu, W.-H. Lai, Y.-X. Wang and H.-K. Liu, *Adv. Mater.*, 2025, **37**, 2419089.
160 M. S. Syali, D. Kumar, K. Mishra and D. K. Kanchan, *Energy Storage Mater.*, 2020, **31**, 352–372.
161 W. Gao, L. Su, Y. Yu, Y. Lu, X. Liu, Y. Peng, X. Xiong, J. He, Y. Chen and Y. Wu, *Angew. Chem., Int. Ed.*, 2024, **63**, e202412287.
162 G. Nikiforidis, M. C. M. Van De Sanden and M. N. Tsampas, *RSC Adv.*, 2019, **9**, 5649–5673.
163 N. Tanibata, M. Deguchi, A. Hayashi and M. Tatsumisago, *Chem. Mater.*, 2017, **29**, 5232–5238.
164 G. Sun, Y. Ma, H. Zhang, S. Wu, S. Chu, S. Passerini and Y. Ma, *Adv. Energy Mater.*, 2025, e03756.
165 J. Yue, F. Han, X. Fan, X. Zhu, Z. Ma, J. Yang and C. Wang, *ACS Nano*, 2017, **11**, 4885–4891.
166 S. Geng, B. Yuan, X. Zhao, Q. Xu, Y. Wang, Z. Ouyang, S. Tang, S. Wang, C. Zhang, Q. Chen, M. Liao, B. Wang, C. Zhao, W. Jin, Z. Li, T.-N. Ye, X. Gong, H. Peng and H. Sun, *Nature*, 2026, **649**, 353–359.
167 J. Huang, X. An, Z. Cheng, J. Jiang, Y. Bai, H.-K. Liu, J. Peng, M. Wu, S.-X. Dou, X. Sun and C. Wu, *J. Am. Chem. Soc.*, 2025, **147**, 46594–46607.
168 J. Huang, X. An, Z. Cheng, L. Li, S.-X. Dou, H.-K. Liu and C. Wu, *Nat. Commun.*, 2025, **16**, 8586.